Neuron

Article

Identification of the velum interpositum as a meningeal-CNS route for myeloid cell trafficking into the brain

Graphical abstract

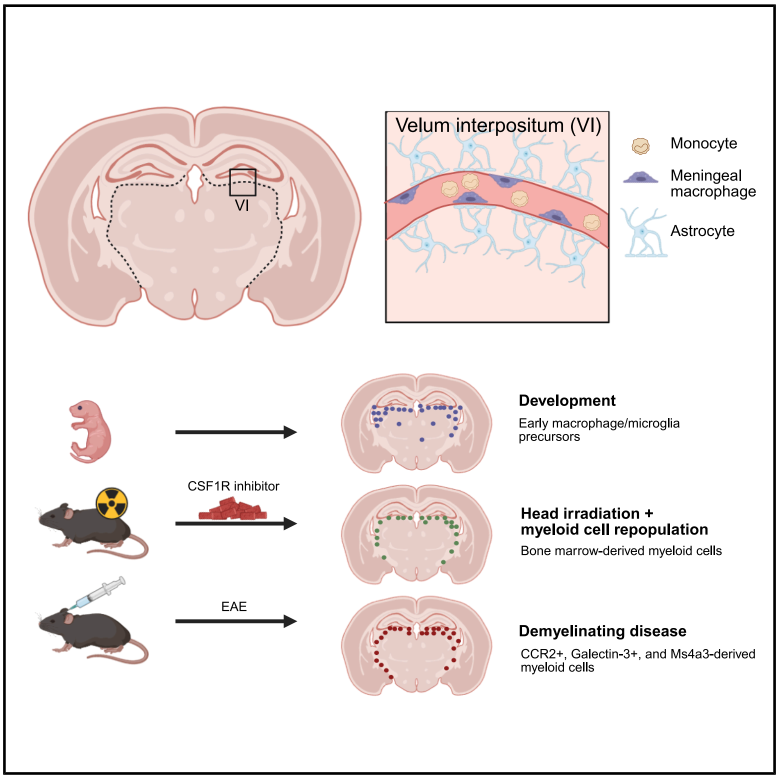

Authors

Lindsay A. Hohsfield, Sung Jin Kim,
Rocio A. Barahona, ..., Xiangmin Xu,
Thomas E. Lane, Kim N. Green

Correspondence

lhohsfie@uci.edu (L.A.H.),
kngreen@uci.edu (K.N.G.)

In brief

Hohsfield et al. reveal a novel gateway for immune cells to enter the brain: the velum interpositum. This structure serves as a crucial entry point for myeloid cells under various brain states. The discovery sheds light on neuroimmune interactions and may have significant implications for understanding and treating neurological diseases.

Highlights

- The velum interpositum (VI) is a site for myeloid cell entry into the murine brain
- The VI is a leptomeningeal extra-parenchymal structure
- The VI contains meningeal macrophages and peripheral myeloid cells
- Distinct myeloid cells utilize the VI during development and demyelinating disease

Hohsfield et al., 2025, Neuron *113*, 1–19

https://doi.org/10.1016/j.neuron.2025.05.004

CellPress

Please cite this article in press as: Hohsfield et al., Identification of the velum interpositum as a meningeal-CNS route for myeloid cell trafficking into the brain, Neuron (2025), https://doi.org/10.1016/j.neuron.2025.05.004

Neuron

CellPress

Article

Identification of the velum interpositum as a meningeal-CNS route for myeloid cell trafficking into the brain

Lindsay A. Hohsfield,[1,2,*] Sung Jin Kim,[1,2] Rocio A. Barahona,[1,2] Caden M. Henningfield,[1,2] Kimiya Mansour,[1,2] Kristen D. Vallejo,[1,2] Kate I. Tsourmas,[1,2] Nellie E. Kwang,[1,2] Yasamine Ghorbanian,[3,4] Julio Alejandro Ayala Angulo,[3,4] Pan Gao,[6,7] Collin Pachow,[4] Matthew A. Inlay,[3,4] Craig M. Walsh,[3,4] Xiangmin Xu,[6,7] Thomas E. Lane,[1,5] and Kim N. Green[1,2,8,*]

[1]Department of Neurobiology and Behavior, University of California, Irvine, Irvine, CA 92697, USA
[2]Institute for Memory Impairments and Neurological Disorders, University of California, Irvine, Irvine, CA 92697, USA
[3]Sue and Bill Gross Stem Cell Research Center, University of California, Irvine, Irvine, CA 92697, USA
[4]Department of Molecular Biology and Biochemistry, University of California, Irvine, Irvine, CA 92697, USA
[5]Center for Virus Research, University of California, Irvine, Irvine, CA 92697, USA
[6]Department of Anatomy and Neurobiology, University of California, Irvine, Irvine, CA 92697, USA
[7]Center for Neural Circuit Mapping (CNCM), University of California, Irvine, Irvine, CA 92697, USA
[8]Lead contact
*Correspondence: lhohsfie@uci.edu (L.A.H.), kngreen@uci.edu (K.N.G.)
https://doi.org/10.1016/j.neuron.2025.05.004

SUMMARY

The borders of the central nervous system (CNS) host a repertoire of immune cells and mediate critical neuro-immune interactions, including the infiltration of peripheral myeloid cells into the CNS. Despite the fundamental role of leukocyte infiltration under physiological and pathological conditions, the neuroanatomical route of cell entry into the brain remains unclear. Here, we describe a specialized structure underneath the hippocampus, the velum interpositum (VI), that serves as a site for myeloid cell entry into the CNS. The VI functions as an extra-parenchymal leptomeningeal extension containing distinct myeloid cells subsets. Fate-mapping studies confirm meningeal and peripheral myeloid cell occupancy within the VI. Additionally, we highlight the distinct use of this route in the developing, irradiated, and demyelinating disease brain, indicating that myeloid cell trafficking through the VI could have important clinical implications for neurological disease.

INTRODUCTION

The central nervous system (CNS) hosts an array of myeloid cells that play integral roles in health and disease.[1] Microglia serve as the brain parenchyma's resident myeloid cells, responsible for immune surveillance, pathogen removal, and tissue homeostasis.[2,3] Choroid plexus, perivascular, and meningeal macrophages are the primary tissue-resident macrophages at these distinct interfaces between the CNS and periphery—known collectively as CNS-associated macrophages or border-associated macrophages (BAMs).[4–7] These gateways to the CNS serve as barriers to control molecular/cellular exchange and access to the brain, implicating BAMs in immune surveillance, including immune cell infiltration and antigen presentation.[4,8] Microglia are long-lived cells maintained by slow and local self-renewal without contributions from bone marrow (BM)-derived cells.[9–12] BAMs also originate from an embryonic yolk sac progenitor, with the exception of stromal choroid plexus and dural macrophages, which are replenished by BM-derived cells in adulthood.[13–15] Recent studies have highlighted the distinct transcriptional and molecular signals that shape CNS macrophage niches.[7,16]

Microglia rely on colony-stimulating factor 1 receptor (CSF1R) signaling for development and maintenance, and methods that inhibit CSF1R signaling have afforded researchers with remarkable tools to study microglia biology.[17–19] Following genetic or pharmacological depletion, microglia can arise from distinct sources (with distinct repopulating kinetics) depending on the ablation method and brain conditions.[17,20–31] We recently identified an approach achieving ∼75%–99% replacement of microglia with BM-derived donor cells, significantly improving traditional BM transplant strategies (∼10%–30% replacement).[9,20,32–35] Given the potential of donor monocytes for microglial replacement therapies,[23,36–38] we applied this approach to gain insight into myeloid cell entry into the brain.

The two most studied routes of peripheral cell trafficking into the brain are the blood-brain barrier (BBB) and the

Please cite this article in press as: Hohsfield et al., Identification of the velum interpositum as a meningeal-CNS route for myeloid cell trafficking into the brain, Neuron (2025), https://doi.org/10.1016/j.neuron.2025.05.004

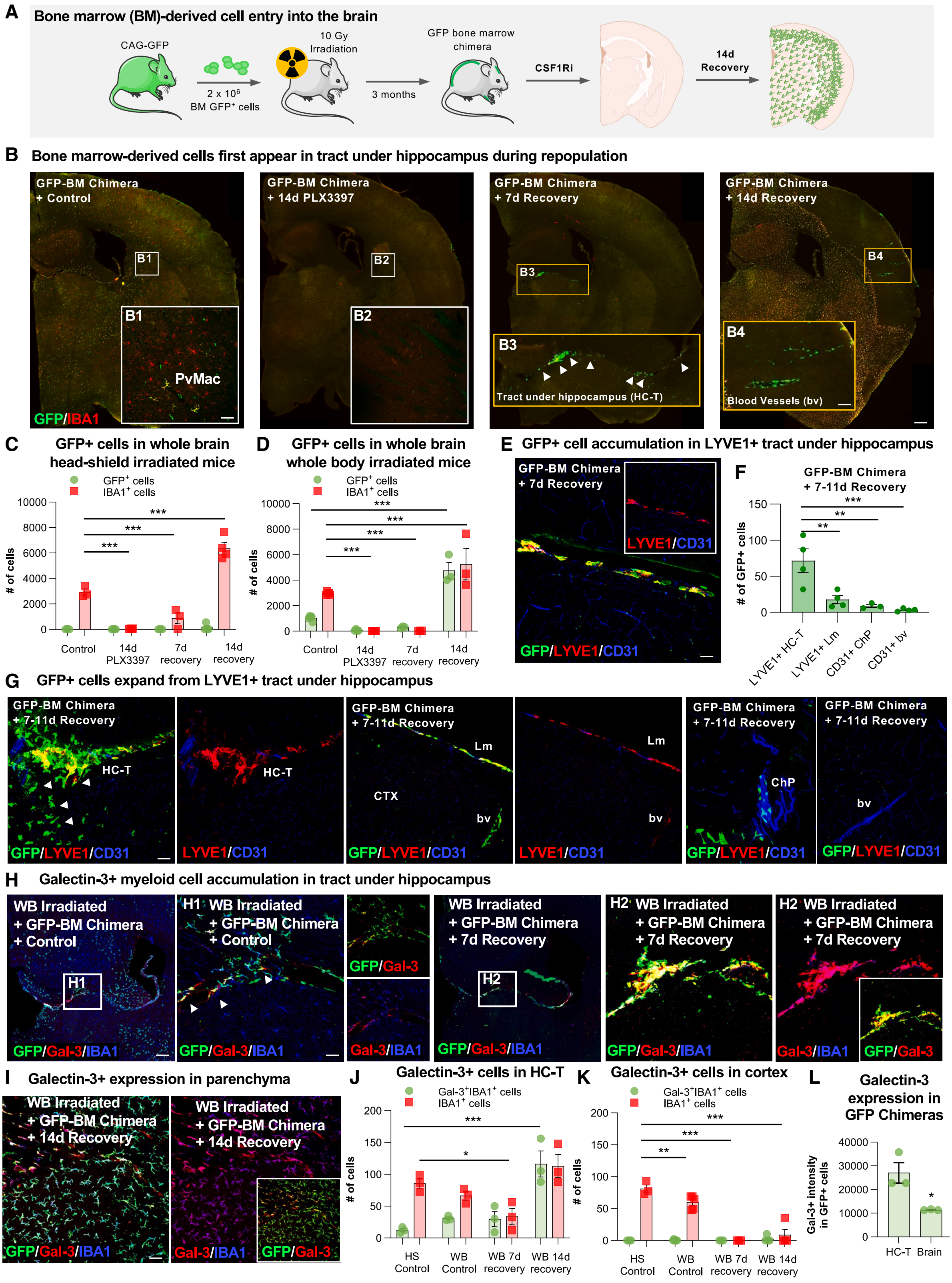

(legend on next page)

choroid plexus. In BBB trafficking, immune cell migration occurs at post-capillary venules and involves selectin-dependent leukocyte rolling, leukocyte adhesion/arrest, and diapedesis across the endothelium. The choroid plexus, with its fenestrated and non-continuous vasculature, results in a leaky interphase between the blood and stroma; however, cell migration from the stroma to the brain remains unclear. Two less studied routes of peripheral cell brain entry involve leptomeningeal vessels and meningeal lymphatics and/or glymphatics.[39,40] A recent review on mechanisms of myeloid cell entry into the CNS provides insight into the differential factors (e.g., development, anatomy, and accessibility) of CNS macrophage niches that contribute to compartment-specific myeloid cell infiltration.[41]

Under neuroinflammatory conditions, such as experimental autoimmune encephalomyelitis (EAE), T cells crawl along pial veins, transmigrate across meningeal vascular structures to reach the subarachnoid space (SAS), and encounter antigen-presenting cells, to become activated and migrate across the glia limitans into the CNS parenchyma.[42,43] Emerging studies reveal direct brain-meningeal interactions, including vascular channels and arachnoid cuff exit (ACE) points, which enable myeloid cell migration from the skull BM to the brain surface and dura mater to the SAS, respectively.[44–46] While these studies provide evidence that the leptomeninges represent a site for immune cell entry into the parenchyma, it remains unclear how cells leave the SAS, pass the glia limitans and migrate into the brain parenchyma.[40,47]

In this study, we identify a specialized structure projecting into the extra-parenchymal space, the velum interpositum (VI). We provide evidence that the VI serves as an extension of the leptomeninges and route for myeloid cell entry into the brain. Fate-mapping study data confirm meningeal myeloid cell occupancy within the VI, providing an important connection between meningeal and brain interactions. We uncover the utility of the VI during non-irradiation and non-repopulation conditions, including demyelinating disease. Inhibition of CSF1R-dependent cells in the meninges and VI delays onset and peak of demyelinating disease, implicating an important role of these cells and the meningeal-VI route under pathological conditions. This study expands our understanding of basic myeloid cell biology and trafficking into the CNS and provides important implications for demyelinating diseases and the development of future therapies.

RESULTS

BM-derived cells first appear in a structure under the hippocampal formation during CNS myeloid cell replacement

Whole-body (WB) irradiation/BM transplant followed by CSF1R inhibitor (CSF1Ri) depletion and withdrawal results in brain-wide (∼85%–99%) and long-term (>10 months post-transplant) peripheral myeloid cell engraftment in the CNS.[20] To study the dynamics of monocyte engraftment into the brain, we generated GFP$^+$ BM chimeric mice using this approach and performed immunohistochemical evaluations to assess critical areas of early GFP$^+$ cell entry into the brain. Consistent with previous studies showing BM-derived cell infiltration following exposure to irradiation,[32] we observed that ∼35% of brain IBA1$^+$ cells were GFP$^+$ in WB-irradiated control mice, indicative of peripheral/BM origins (Figures 1A–1C, 1B1, 1D, S1A, and S1D). We find that the majority of GFP$^+$ cells appeared to be perivascular macrophages or macrophages located within blood vessel-like structures, consistent with studies showing BM-derived myeloid cells replace perivascular macrophages following irradiation[13,48] (Figure 1B1). Fourteen-day CSF1Ri (PLX3397) treatment eliminated all myeloid cells in WB-irradiated brains (Figures 1B, 1B2, and 1D), underscoring their dependence on CSF1R signaling once established in parenchymal spaces.

While examining the dynamics of infiltrating BM-derived myeloid cells into the CNS during the early stages of repopulation (i.e., 5–7-day recovery), we noted extensive coverage and accumulation of GFP$^+$IBA1$^+$ cells in a structure running underneath the hippocampal formation (Figures 1B, 1B3, and S1F). By 14-day recovery, all repopulating IBA1$^+$ cells are GFP$^+$ and exhibit a distinct radial migratory pattern (Figures 1B and S1H). At this time point, we also observe GFP$^+$ cells within blood-vessel-like structures, indicating again BM cell replacement of perivascular macrophages (Figure 1B4). Despite this replacement, GFP$^+$ cells do not appear to be migrating out from blood vessels to repopulate the brain parenchyma (Figure 1B4), but rather from the structure under the hippocampal formation (Figure 1B3). Staining for lymphatic vessel endothelial hyaluronan receptor 1 (LYVE1), a marker for lymphatic endothelial cells, and CD31, a marker for endothelial cells, reveals that this tract contains GFP$^+$ and LYVE1$^+$ cells (Figure 1E). Further, examination of brain sections shows that repopulating GFP$^+$ cells expand from the LYVE1$^+$ tract under the hippocampus, but not

Figure 1. BM-derived cells first appear in a structure under the hippocampal formation during CNS myeloid cell replacement
(A) Generation of BM GFP$^+$ chimeras.
(B) Whole-brain images of GFP$^+$ (green) and IBA1$^+$ (red) cells; insets show higher-resolution images of GFP$^+$ cells in a tract under the hippocampus (HC-T, arrows) and perivascular spaces.
(C and D) Quantification of GFP$^+$ and IBA1$^+$ cells.
(E) Confocal image of LYVE1$^+$ (red) and CD31$^+$ (blue) staining in the HC-T where GFP$^+$ cells accumulate at 7-day recovery.
(F) Quantification of GFP$^+$ cells in the LYVE1$^+$ HC-T, LYVE1$^+$ leptomeninges (Lm), CD31$^+$ choroid plexus (ChP), and CD31$^+$ blood vessels (bv).
(G) Confocal images of LYVE1$^+$ (red) and CD31$^+$ (blue) structures where GFP$^+$ cells expand into the CNS between 7- and 11-day recovery.
(H and I) Images of GFP$^+$ (green), galectin-3$^+$ (Gal-3, red), and IBA1$^+$ (blue) cells in the HC-T.
(J and K) Quantification of IBA1$^+$ and Gal-3$^+$IBA1$^+$ cells.
(L) Quantification of Gal-3$^+$ expression intensity in GFP$^+$ BM cells.
Data are mean ± SEM ($n = 3$–5; 3+ groups: two-way ANOVA with Dunnett post hoc; 2 groups: t test; $^*p < 0.05$, $^{**}p < 0.01$, $^{***}p < 0.001$). PvMac, perivascular macrophages. Scale bars: ∼200 μm for (B); ∼100 μm (H); ∼70 μm for (B1) and (B2); ∼50 μm for (B3) and (B4); ∼30 μm for (G), (H1), (H2), and (I); ∼10 μm (E).
See also Figure S1.

Please cite this article in press as: Hohsfield et al., Identification of the velum interpositum as a meningeal-CNS route for myeloid cell trafficking into the brain, Neuron (2025), https://doi.org/10.1016/j.neuron.2025.05.004

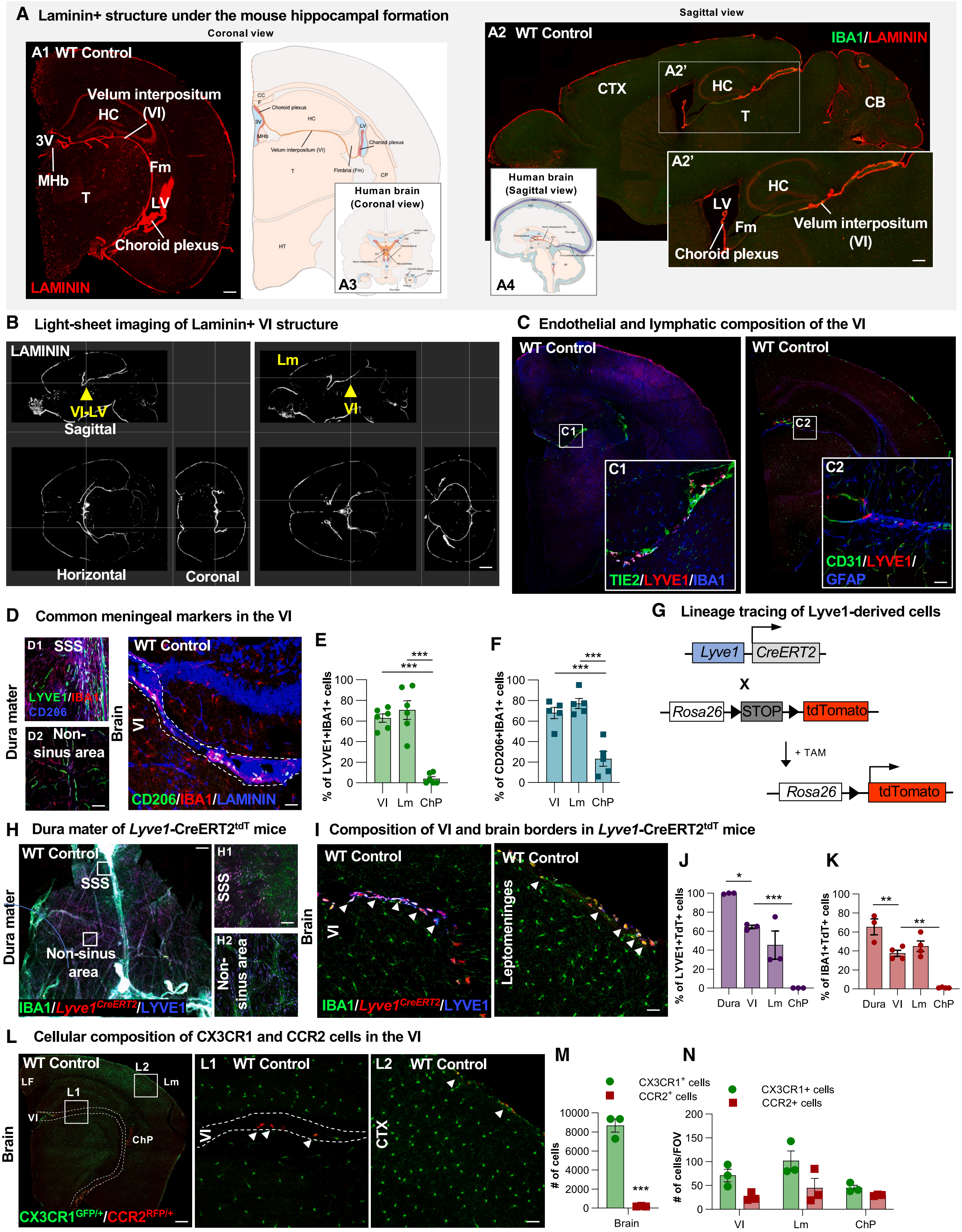

(legend on next page)

from other brain border sites, including the leptomeninges (i.e., outer surface of the brain), perivascular spaces, or the choroid plexus (Figures 1F and 1G).

Recent single-cell RNA sequencing studies show that *Lgals3*, which encodes for Galectin-3, is upregulated in disease-associated microglia and other subsets.[49–51] However, we recently identified MAC2/galectin-3 as a marker for peripheral immune cells, highlighting its expression in myeloid cells that infiltrate the brain following intracranial infection with the neurotropic JHM strain of mouse hepatitis virus (JHMV) infection and BM transplant.[52] Here, we observe that GFP$^+$IBA1$^+$ cells that first appear in the tract under the hippocampus are galectin-3$^+$ (Gal-3$^+$) (Figures 1H–1K). While BM-derived cells retain Gal-3 staining as they enter and engraft the CNS parenchyma, cells within the tract exhibit elevated Gal-3 expression compared with those outside of the tract (Figure 1L). Taken together, these data indicate that irradiation allows for the entry of BM-derived cells through specific anatomical locations and routes, rather than an influx through damaged blood vessels. Thus, we hypothesized that the influx of BM-derived cells into the CNS utilizes a specialized structure running underneath the hippocampus.

Identification of the VI

As both the leptomeninges and the tract under the hippocampus stained positive for LYVE1, we next examined whether this tract could be part of the meningeal compartment. The meninges are known as a protective membrane covering the brain; however, recent studies have highlighted this structure's ability to penetrate deeper cerebral territories.[53] In the adult brain, the meninges not only form the roof of the ventricular system, but also includes a major projection underneath the hippocampal formation, which connects to the choroid plexus stroma.[54,55] Immunohistochemistry using LAMININ, a marker commonly used to label the leptomeninges, confirmed the presence of a LAMININ-enriched structure running between the hippocampus and thalamus in control murine brains—the same site we observed GFP$^+$ peripheral cell entry in chimeric mice (Figures 2A and 2A1).

Further anatomical exploration of this structure suggested that it may represent an extension of the meninges. The tela choroidea—a double-layered fold of pia mater—adheres to the ependyma of the ventricle, forming the roof of the ventricle and giving rise to the choroid plexus. In humans, the space between the two layers of the tela choroidea is referred to as the VI[56–58] (Figures 2A3 and S2A). Previous microsurgical study of the human brain describes the VI as a membrane that lies over the thalamus, which is continuous with the choroid plexus of the lateral ventricles as well as with the pia/arachnoid of the cerebellum and inferior surface of the parietal/occipital lobes (Figures 2A4 and S2A).[59] Thus, this structure under the murine hippocampus aligns with that of the VI in humans but has not been extensively explored or characterized in mice.

To further explore this structure, we next performed whole-brain structural imaging on wild-type (WT) mouse brains using light-sheet microscopy. Videos S1 and S2 and a series of maximum intensity projection representative images display the geospatial distribution of the VI spanning whole brains in coronal, sagittal, and horizontal planes (Figures 2B, S2B, and S2C). Whole-brain imaging reveals that a LAMININ$^+$ projection running under the hippocampal formation connects the third ventricle to the lateral ventricle (as seen in the coronal plane; Figures 2B and S2D) as well as connects the leptomeninges to the lateral ventricle (as seen in the sagittal plane; Figures 2B and S2E).

Since the VI is known to be highly vascularized with internal cerebral arterioles and veins[58] and given that the meninges are associated with an extensive vascular network, we next stained for vascular and lymphatic endothelial cell markers, TIE2 and LYVE1, respectively. Here, we observe both TIE2$^+$ and LYVE1$^+$ staining within the murine VI (Figures 2C, 2C1, and 2C2), although LYVE1$^+$ staining appears cellular. LYVE1 is a well-known marker of resident meningeal and perivascular macrophages; thus, our data indicate that BAMs are dispersed in this structure.[60]

Expression of mannose receptor CD206, encoded by *Mrc1*, and LYVE1 has been identified in discrete subsets of BAMs.[6,13,61–63] Here, we observe that CD206$^+$IBA1$^+$ and LYVE1$^+$IBA1$^+$ cells are present in both the dural sinuses (i.e., the superior sagittal sinus

Figure 2. Identification of the VI

(A) Coronal and sagittal sections of wild-type (WT) mouse brains stained for IBA1 (green) and LAMININ (red); inset shows higher-resolution image of VI (A2′). Schematics indicate location of the VI in mouse and human brains.

(B) Whole-brain light-sheet imaging of LAMININ; arrows highlight connections between the Lm, VI, and LV.

(C) Images of endothelial (TIE2, CD31; green), lymphatic/meningeal (LYVE1; red), and glial cells (IBA1, GFAP; blue) in the VI; insets indicate the VI is composed of endothelial cells, meningeal macrophages, surrounded by astrocytes.

(D) Confocal images of IBA1$^+$ (red), LYVE1$^+$ (green), CD206$^+$ (blue or green) cells in the dura mater and VI (LAMININ, blue). Dotted white lines illustrate the location of the VI.

(E and F) Quantification of LYVE1$^+$IBA1$^+$ (E) and CD206$^+$IBA1$^+$ (F) cells in the VI, Lm, and ChP.

(G) Schematic of lineage labeling in *Lyve1*$^{\text{CreERT2}}$/tdT mice; tamoxifen administration causes tdT expression in *Lyve1* cells.

(H and I) Images of IBA1$^+$ (green), *Lyve1*$^{\textit{CreERT2}}$/tdT (red), and LYVE1$^+$ (blue) cells in the dura mater (H), VI and Lm (I) of control *Lyve1*$^{\textit{CreERT2}}$/tdT mice; insets show cells in the SSS and non-sinus areas of the dura. Arrows highlight cells within the VI and Lm.

(J and K) Quantification of tdTomato$^+$ cells in the dura mater, VI, Lm, and ChP.

(L) Images of *Cx3cr1*$^{\text{GFP/+}}$/*Ccr2*$^{\text{RFP/+}}$ mouse brains. Dotted white lines indicate the VI. White insets show *Cx3cr1*$^{\text{GFP/+}}$ and *Ccr2*$^{\text{RFP/+}}$ cells (arrows) in the VI and Lm.

(M and N) Quantification of *Cx3cr1*$^{\text{GFP/+}}$ and *Ccr2*$^{\text{RFP/+}}$ cells in the cortex (M), VI, Lm, and ChP (N).

Data are mean ± SEM ($n = 3$; two-way ANOVA with Šidák's post hoc; $^*p < 0.05$, $^{**}p < 0.01$, $^{***}p < 0.001$). HC, hippocampus; MHb, medial habenula; Fm, fimbria; T, thalamus; LV, lateral ventricle; CTX, cortex; CB, cerebellum; 3V, third ventricle; CC, corpus callosum; F, fornix; HT, hypothalamus; CP, caudoputamen; CN, caudate nucleus; ICV, internal cerebral vein; PG, pineal gland; H, habenula; 4V, fourth ventricle; SSS, superior sagittal sinus. Scale bars: ∼700 μm for (B); ∼200 μm for (A1), (A2), (C), (H), and (L); whole brains and dura mater); ∼100 μm for (A2′), (H1), and (H2); ∼70 μm for (C1), (C2), (D1), and (D2); ∼50 μm for (D), (L1), and (L2); ∼30 μm for (I).

See also Figures S2 and S3.

Please cite this article in press as: Hohsfield et al., Identification of the velum interpositum as a meningeal-CNS route for myeloid cell trafficking into the brain, Neuron (2025), https://doi.org/10.1016/j.neuron.2025.05.004

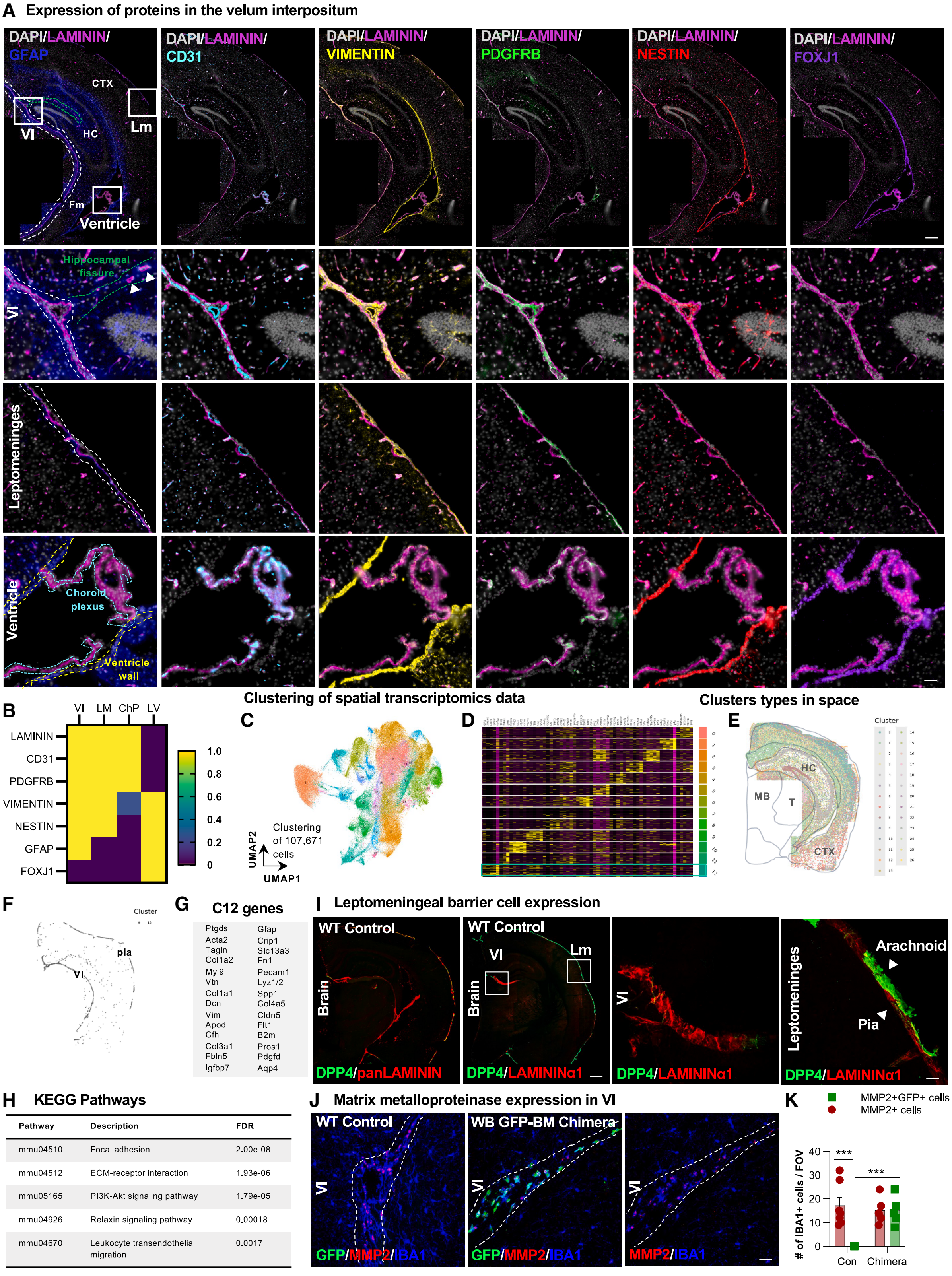

Pathway	Description	FDR
mmu04510	Focal adhesion	2.00e-08
mmu04512	ECM-receptor interaction	1.93e-06
mmu05165	PI3K-Akt signaling pathway	1.79e-05
mmu04926	Relaxin signaling pathway	0.00018
mmu04670	Leukocyte transendothelial migration	0.0017

(legend on next page)

[SSS]) and throughout the non-sinus areas of dura mater of the meninges (Figures 2D1 and 2D2). Moreover, we observe deposition of CD206$^+$IBA1$^+$ and LYVE1$^+$IBA1$^+$ cells within the VI (Figures 2D–2F and S3A). Using lineage tracing studies with *Lyve1*^{CreERT2} crossed to tdTomato (tdT) reporter mice, we show that *Lyve1*-derived cells markedly populate the dura mater, comprising ~65% of all meningeal IBA1$^+$ myeloid cells (Figures 2H–2K). LYVE1$^+$ cell staining is prominent within the VI and leptomeninges (composed of pia and arachnoid meningeal layers) with ~38% and ~45% of myeloid cells labeled with tdT (Figures 2I–2K), respectively. No or few *Lyve1*-derived cells are found in the choroid plexus (Figures 2J, 2K, and S3B). Statistical analysis reveals that the dura, VI, and choroid plexus exhibit distinct distribution of *Lyve1*-derived cells; however, the distribution of these cells in the VI and leptomeningeal are comparable.

To explore whether the VI potentially receives peripheral input, we next sought to investigate the presence of *Cx3cr1* and *Ccr2* myeloid cells within this structure. To accomplish this, brain and meningeal tissue was collected from Cx3cr1$^{GFP/+}$Ccr2$^{RFP/+}$ dual reporter mice; in these mice, red fluorescent protein (RFP) is expressed in CCR2$^+$ cells, and green fluorescent protein (GFP) is expressed in CX3CR1$^+$ cells. In the meninges of *Cx3cr1*$^{GFP/+}$/*Ccr2*$^{RFP/+}$ mice, *Cx3cr1*^{GFP}cells are distributed throughout the dura mater—whereas *Ccr2*^{RFP} are found exclusively in the sinuses (Figures S3C–S3E). In the brains of *Cx3cr1*$^{GFP/+}$/*Ccr2*$^{RFP/+}$ mice, we observe prominent *Cx3cr1*$^{GFP+}$ and *Ccr2*$^{RF2+}$ cell accumulation in the VI (Figure 2L1), leptomeninges (Figure 2L2), longitudinal fissure, and choroid plexus (Figures 2L–2N), highlighting the potential myeloid cell trafficking route from the meninges into the brain via the VI. Together, these data provide evidence that the structure we identify under the hippocampus is a vascularized structure that shares a similar cellular composition profile to the meninges, i.e., it is filled with BAMs and peripheral myeloid cells.

Molecular characterization of the VI—A leptomeningeal extension into the extra-parenchymal spaces of the brain

To visualize the gene and protein expression patterns and identify cellular and molecular constituents of the VI, we performed high-plex single-cell resolution *in situ* analysis of protein and RNA by spatial molecular imaging.[64] Frozen WT brains were analyzed using the CosMx Spatial Molecular Imager platform (Figure S4A), providing spatial proteomic and transcriptional information while preserving native cellular architecture. We again demonstrate that the VI is enriched for LAMININ, a known constituent of endothelial basement membranes (Figure 3A). Focusing on a selected field of view (FOV) that captured the LAMININ$^+$ VI, the LAMININ$^+$ leptomeninges and the lateral ventricle (Figure S4B), we identified several intermediate filament proteins that distinguish these specific and distinct brain regions. Glial fibrillary acidic protein (GFAP) is expressed in cells that surround the VI, within the leptomeninges, along the walls of the lateral ventricle, and within the corpus callosum. Cells positive for VIMENTIN, a protein expressed in mesenchymal cells—including fibroblasts, and NESTIN, a protein expressed in neuroepithelial stem cells, are prevalent in both the VI, leptomeninges, and lateral ventricle (Figures 3A and 3B). In contrast, staining for CD31, a glycoprotein expressed on the vascular endothelium, as well as platelet-derived growth factor receptor beta (PDGFRβ), a growth factor receptor highly expressed in pericytes, is only found in the VI and leptomeninges, but not within the walls of the ventricles (although it is present in some cells in the choroid plexus) (Figures 3A and 3B). Interestingly, we observe CD31, VIMENTIN, and PDGFRβ expression within LAMININ$^+$ structures in the hippocampal fissure (Figure 3A). As expected, we found high expression of FOXJ1, a regulator of motile cilia, in the ependymal layer of the lateral ventricle, where cilia are essential for cerebrospinal fluid movement, but no expression in the VI or leptomeninges[65] (Figures 3A and 3B). These data highlight the unique molecular and cellular profile of the VI from other brain border interfaces.

We next applied spatial transcriptomics to spatially resolve gene expression changes within the murine brain and identify distinct genes expressed in the VI. Across all sections (207 total FOVs, ~69 FOVs/brain section), we captured 107,671 cells with a mean of ~400 transcripts per cell. All coronal brain slices contained the VI and surrounding hippocampal and cortical tissue. Unbiased cell clustering identified 27 transcriptionally distinct clusters within our dataset (Figure 3C). We annotated these clusters based on the expression of known marker genes and unbiased cluster marker gene detection (Figures 3D and S4C).

Figure 3. Characterization of the VI—A leptomeningeal extension into the extra-parenchymal spaces of the brain

(A) Immunofluorescence images of WT mouse brains showing GFAP, CD31, VIMENTIN, PDGFRβ, NESTIN, FOXJ1, DAPI, and LAMININ expression in the VI, Lm, and LV.

(B) Heatmap quantifying protein expression in (A) as visualized across 3 brains; high expression = 1.0; moderate = 0.5; low/no expression = 0.0.

(C) Uniform manifold approximation and projection (UMAP) of 107,671 cells across WT hemibrains ($n = 3$), identifying 27 clusters based on gene expression and anatomical location in x-y space.

(D) Heatmap of top 5 genes enriched in each cluster, highlighting cluster 12 (C12) as a VLMC cluster.

(E) Schematic of clusters in XY space accompanied by a depiction of major brain areas.

(F) Schematic of cluster 12 plotted in XY space, highlighting the enrichment of this cluster in the VI and Lm.

(G) Top 28 genes enriched in cluster 12.

(H) Gene Ontology analysis of differentially expressed genes (DEGs) in cluster 12, highlighting pathways involved in extracellular matrix-receptor interactions, adhesion, and migration.

(I) Confocal images of DPP4 (green) and panLAMININ or LAMININα1 (red) in WT brains.

(J) Confocal images of GFP$^+$ (green), MMP2$^+$ (red), and IBA1$^+$ (blue) staining in the VI (white dotted lines) of WT and GFP-BM chimeric mice.

(K) Quantification of (J).

Data are mean ± SEM ($n = 5$–7; two-way ANOVA with Fisher's least significant difference (LSD) post hoc; $^{***}p < 0.001$). MMP2, matrix metalloproteinase 2.

Scale bars: ~200 μm for (A, top) and (I, whole brains); ~50 μm for (A, bottom); ~30 μm for (I) and (J).

See also Figure S4.

Visualization of these clusters in X-Y space reveals one cluster (cluster 12) that aligns spatially with the location of the VI and leptomeninges (Figures 3E, 3F, and S4D), providing evidence that the VI shares transcriptional resemblance with the leptomeninges. The top enriched genes in cluster 12 include those previously identified in vascular leptomeningeal cells (VLMCs) (*Dcn*, *Col1a2*, *Col1a1*, *Col3a1*, *Vtn, Apod*, *Pecam1*, *Cldn5*, *Flt1*, *Acta2*, and *Tagln*), including markers for collagens and blood-vessel-associated cells[66–71] (Figure 3G). In line with our data, previous studies have shown that VLMCs are mainly located in the pia and arachnoid membranes of the brain.[66,72] Moreover, several cluster 12 genes and/or associated proteins have been identified in the leptomeninges, including in arachnoid barrier/fibroblasts (*Ptgds*, *Vim*, and *Tagln*),[73–75] perivascular macrophages/fibroblasts (*Spp1*)[68,76] and meningeal fibroblasts (*Col1a2*, *Col1a1*, and *Cfh*).[73,77] We also found genes associated with astrocytes (*Gfap* and *Aqp4*), which likely corresponds with the glia limitans.[78] Pathway analysis of the top enriched genes in cluster 12 implicate several pathways involved in cell adhesion, migration, and signaling, including *focal adhesion*, extracellular matrix (*ECM)-receptor interaction*, *P13K-Akt signaling*, *Relaxin signaling*, and *leukocyte transendothelial migration* (Figure 3H). Together, these data indicate that the VI is a leptomeningeal extension where several cell types exhibit spatial colocalization, alongside a network of collagens and extracellular matrix components, vascular endothelium, basement membrane, and glial cells.

Previous studies have described molecularly distinct compartments of the meninges based on differential expression of basement membrane laminins[79] and the presence of transcriptionally distinct brain border cells (i.e., meningeal fibroblasts) within different anatomical barriers.[72] To better understand the molecular identity of the VI, we stained brain sections for LAMININα1, a marker that distinguishes pial and arachnoid layers,[79] and dipeptidyl peptidase-4 (DPP4), a marker for arachnoid barrier cells.[72] Here, we observe that DPP4 labels the outer surface of the brain but does not stain the VI. Immunostaining for LAMININα1 specifically labels the outer surface of the brain, as well as the VI (Figure 3I). Staining for other forms of laminin is provided in Figures S4E and S4F. These data provide evidence that the VI consists of pial basement membrane, in alignment with our transcriptional data and previous studies highlighting collagen, laminin, and matrix metalloproteinase (MMP) enrichment in pial fibroblast subclusters.[72,73]

Recent data implicate the ECM in the migration of leptomeningeal macrophages into perivascular spaces.[7] It is well known that upon penetration of the endothelial cell monolayer and basement membrane, extravasating leukocytes must traverse parenchymal basement membrane and glial limitans before entering the brain parenchyma. One of the major enzymes associated with infiltrating leukocytes is MMP2, which exhibits activity at sites of leukocyte penetration of the parenchymal basement membrane.[80] Thus, we hypothesized that if cells utilize the VI for cell migration, then MMP2 expression may be prevalent in this area of the brain. Immunostaining for MMP2 demonstrates that this protein is highly expressed in the VI region and colocalizes with infiltrating GFP$^+$ BM myeloid cells (Figures 3J and 3K). Together, these data indicate that the structure we identify as the VI under the hippocampal formation is a vascularized leptomeningeal structure that serves as a potential route of migration for infiltrating myeloid cells in the brain parenchyma.

The VI as a route for myeloid cell trafficking and entry into the brain

The meninges host an extensive repertoire of immune cells including pools of myeloid cells that, under pathological conditions, can mobilize and accumulate within this CNS border before infiltrating into the parenchyma.[46,81–84] To explore whether the VI serves as a route for myeloid cell mobilization, trafficking, and entry into the brain, we explored two distinct conditions involving myeloid cell CNS colonization or reconstitution:

Utilization of VI during development

Microglia originate from yolk-sac-derived progenitors and migrate to colonize the CNS from embryogenesis (~E9.5) until the end of the second postnatal week.[85–87] While previous data suggest that CX3CR1$^+$ microglial precursors migrate into the brain via blood vessels, and report high densities of these cells near pial and ventricular surfaces prior to cortical distribution,[88,89] the neuroanatomical route of cell entry remains unknown. Here, we evaluated the spatiotemporal features of myeloid cell colonization in the developing mouse brain at different embryonic and early postnatal stages of development: E17, P1, P5, and P9 (Figures 4A–4D). At E17, the most prominent IBA1$^+$ accumulation occurs in areas known in the adult murine brain as the leptomeninges, longitudinal fissure and third ventricle, along with blood vessel-like staining (Figure 4A). In postnatal stages (P1–P9), LAMININ$^+$ staining is present in similar regions, as well as the VI (Figure 4A). At P1, IBA1$^+$ cells are densely packed along the VI, longitudinal fissure, and certain areas of the ventricles, with few in the brain parenchyma (Figures 4A–4D and S5A). At P5 and P9, IBA1$^+$ cells are still present in the VI, but display broader spreading to the thalamus (at P5) and cortex (at P9) (Figures 4A–4D and S5A), mirroring reported spatiotemporal spreading and migratory of microglial colonization. Given the deposition of IBA1$^+$ cells within the VI following primitive BBB formation (~E15.5), these data could also represent the routes by which early BAM precursors begin to occupy and expand within this CNS border niche.[90] A recent study indicates that developing leptomeninges act as an intermediate environmental niche, from which meningeal macrophages migrate into perivascular spaces to give rise to perivascular macrophages postnatally.[7] Future lineage tracing experiments will be necessary to confirm the identity of myeloid cells in the VI during development.

BM-derived myeloid cell entry into the brain parenchyma via the VI following head irradiation

We next explored whether this leptomeningeal structure is utilized by BM-derived myeloid cells to access the adult brain in the absence of CSF1R signaling disruption. Brains of WB irradiated chimeric mice ~10 months post-irradiation were examined, providing extended recovery from BBB disruption.[91] Few GFP$^+$ cells were present in the brain parenchyma (Figures 4E and 4F), but GFP$^+$ cell deposition was prominent within the VI and fimbria, as well as the leptomeninges and choroid plexus (Figures 4E, 4G, 4H, and S5B). GFP$^+$ cell accumulation was also visible in the hippocampal fissure and cortical blood vessels

Please cite this article in press as: Hohsfield et al., Identification of the velum interpositum as a meningeal-CNS route for myeloid cell trafficking into the brain, Neuron (2025), https://doi.org/10.1016/j.neuron.2025.05.004

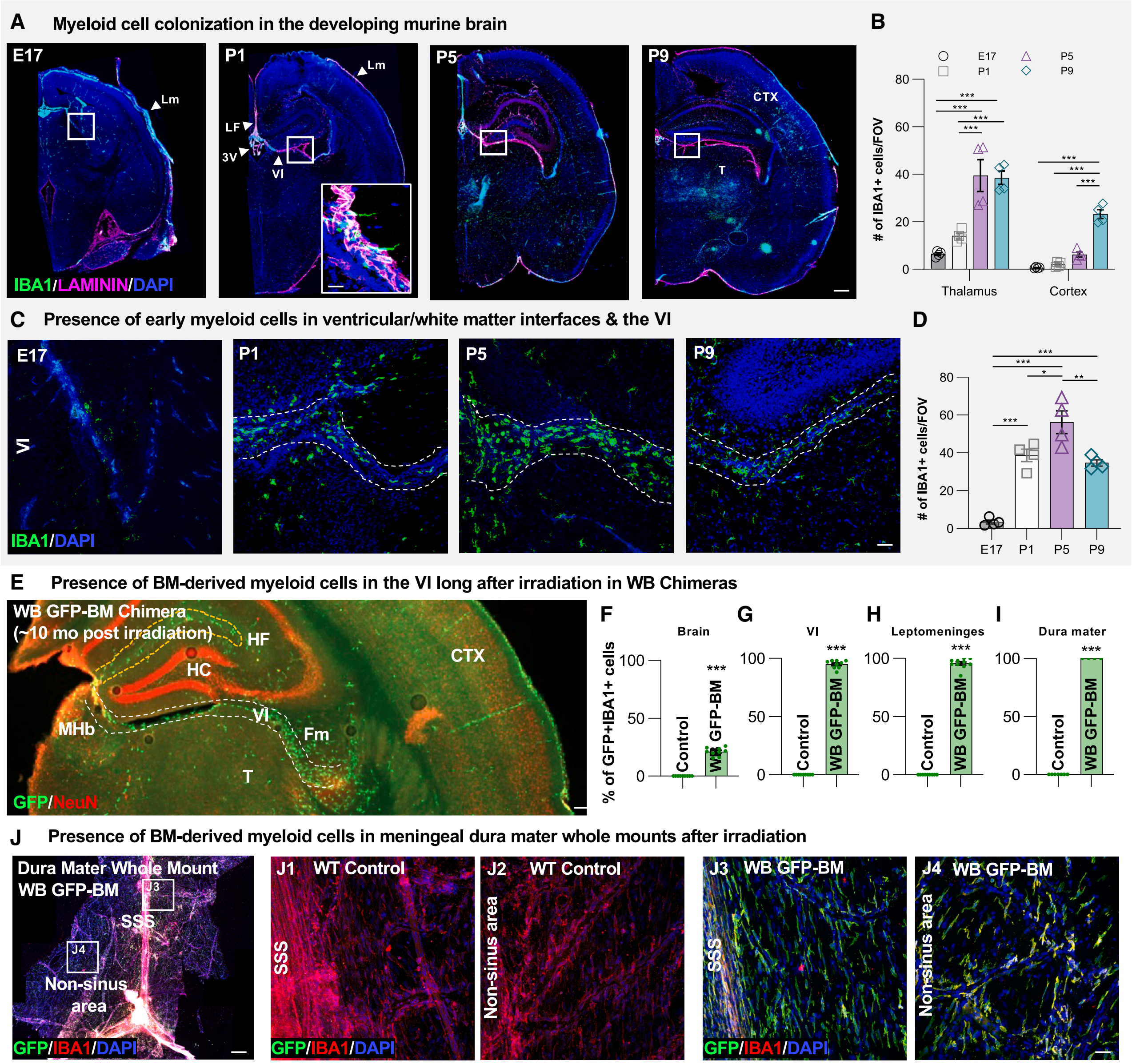

Figure 4. The VI as a route for myeloid cell trafficking and entry into the brain

(A) Whole-brain images of embryonic and early postnatal mouse brains (E17, P1, P5, and P9) stained for IBA1 (green), LAMININ (magenta), and DAPI (blue); inset shows higher-resolution image of IBA1$^+$ cells within this LAMININ$^+$ structure.

(B) Quantification of IBA1$^+$ cells in the thalamus and cortex.

(C) Confocal images of the VI in embryonic and early postnatal mice stained for IBA1 (green) and DAPI (blue).

(D) Quantification of (C).

(E) Whole-brain image of GFP$^+$ BM (green) and NeuN$^+$ (red, to show brain structure) cells in chimeric mice ~10 months post-irradiation. Dotted white lines indicate the VI and dotted yellow lines denote the hippocampal fissure (HF).

(F–I) Quantification of GFP$^+$IBA1$^+$/IBA1$^+$ (%) in the brain, VI, Lm (pia and arachnoid), and dura mater.

(J) Meningeal whole mount and confocal images of GFP$^+$, IBA1$^+$, and DAPI$^+$ cells in the dura mater of WT mice (J1 and J2) and WB-irradiated GFP-BM chimeric mice (J3 and J4).

Data are mean ± SEM (*n* = 3–9; 3+ groups: two-way ANOVA with Tukey's post hoc testing, B and D; and Dunnett post hoc testing, M, 2 groups: t test; **p* < 0.05, ***p* < 0.01, ****p* < 0.001). LF, longitudinal fissure.

Scale bars: ~250 μm for (A); ~200 μm for (J); ~100 μm for (E); ~30 μm (C) and (J1)–(J4).

See also Figure S5.

Please cite this article in press as: Hohsfield et al., Identification of the velum interpositum as a meningeal-CNS route for myeloid cell trafficking into the brain, Neuron (2025), https://doi.org/10.1016/j.neuron.2025.05.004

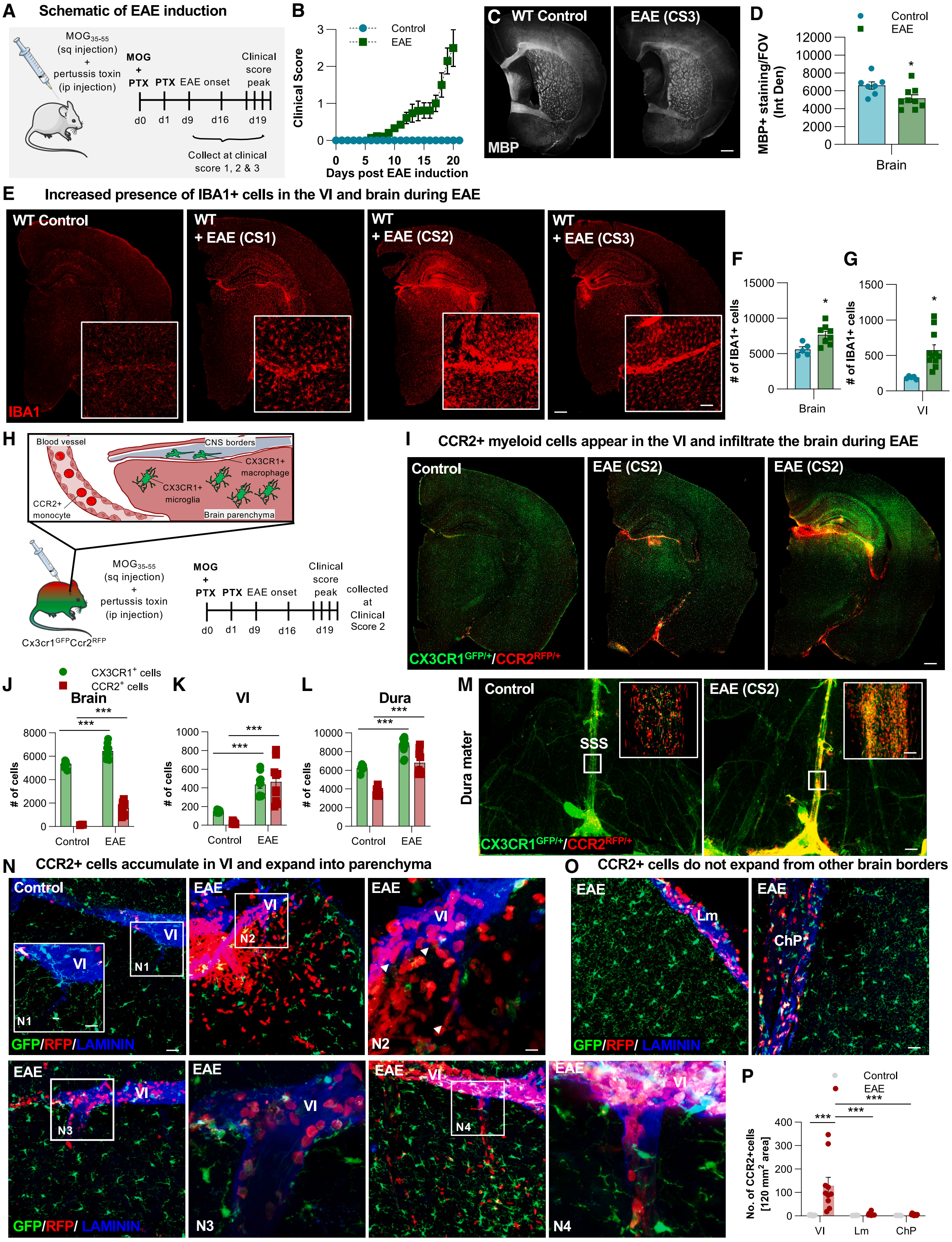

Figure 5. Myeloid cells occupy the VI and utilize this route during demyelinating disease

(A) EAE induction of mice with myelin oligodendrocyte glycoprotein $(MOG)_{35-55}$/complete Freund's adjuvant (CFA) and pertussis toxin (PTX). First signs of paralysis appeared at day 9. Animals were euthanized at clincal scores (CS) 1, 2, and 3 (days 13–20).

(legend continued on next page)

(Figure 4E). Since our data indicate that the VI serves as an extension of the leptomeninges, we next collected dura mater and assessed whether the peripheral myeloid cell makeup of the meninges matched the VI. Here, we observe 100% reconstitution of the meningeal dura mater myeloid cell compartment with BM-derived GFP^+ cells following head irradiation (Figures 4I, 4J, 4J3, and 4J4). No GFP^+ cells are found in the dura mater of non-irradiated control mice (Figures 4J1 and 4J2). These data confirm long-term BM cell replacement of meningeal macrophages post-irradiation, consistent with prior studies,[20,34,92] and highlight a potential connection between the VI and meninges and the VI's role in peripheral myeloid cell trafficking into the CNS under certain experimental conditions.

Myeloid cells occupy the VI and utilize this route during demyelinating disease

To investigate the VI's role in peripheral myeloid cell CNS infiltration under pathological conditions, we employed a mouse model of demyelination—experimental autoimmune encephalomyelitis (EAE). EAE was induced in WT mice and brains collected at clinical scores 1–3 (CS 1–3) to visualize myeloid cell changes across the disease (Figures 5A and 5B). Demyelination was confirmed by loss of myelin basic protein (MBP) immunostaining (Figures 5C and 5D). During EAE, we observed a significant increase in $IBA1^+$ cells in the VI and brain (Figures 5E–5G), with the most pronounced accumulation at CS2 (Figure S6A). Immunostaining for galectin-3 (Gal-3) reveals that $Gal\text{-}3^+IBA1^+$ cells are specifically localized in the VI during EAE and appear to expand into parenchymal spaces from the VI (Figures S6B, S6B1, S6B2, and S6C). Concurrently, we noted extensive accumulation of $Gal\text{-}3^+IBA1^+$ cells in the dura mater, particularly in the SSS (Figures S6D, S6D1, S6D2, and S6E).

We next leveraged two complementary fate-mapping approaches to explore whether peripheral myeloid cells exploit the VI route to enter the brain during demyelinating disease. First, we induced EAE in $Cx3cr1^{GFP/+}Ccr2^{RFP/+}$ dual reporter mice (Figures 5H and S6F). These mice display pronounced $CX3CR1^+$ and $CCR2^+$ cell deposition in the brain, VI, and dura mater at CS2 (Figures 5I–5M). Notably, $CCR2^+$ cells accumulate in other brain borders during EAE (i.e., leptomeninges and choroid plexus); however, appear to only expand into the brain parenchyma from the VI (Figures 5I–5K and S6G–S6J). Co-staining with LAMININ revealed several areas of the VI in which we observe infiltration of $CCR2^+$ cells from the basement membrane components of the VI into the brain parenchyma (Figures S6K–S6M). Using super-resolution microscopy, we capture diverse $CCR2^+$ cell trafficking strategies from the VI into brain parenchymal spaces (Figure 5N), including a massive influx of $CCR2^+$ cells with altered cell morphologies (e.g., thin elongated cells) into the parenchyma at one site (Figure 5N2) and more orderly expansion along small blood vessels at other sites (Figures 5N3 and 5N4). Evaluation of other brain border sites reveals that the VI is a unique site for $CCR2^+$ and $CX3CR1^+$ cell expansion and entry into the brain parenchyma (Figures 5P and S6N), though the mechanism of cell entry (e.g., remodeling or loss of the basement membrane), requires further investigation.

Second, *Ms4a3*^{Cre}-*Rosa*^{TdT} reporter mice, which label granulocyte-monocyte progenitor (GMP) cells and progeny[93] (Figure S7A), were induced with EAE (Figures S7B and S7C). Here, we observe a significant increase in tdT^+, including $tdT^+Gal\text{-}3^+$ cells in the brain parenchyma and VI of EAE mice compared with controls (Figures S7D–S7H). The dura mater of EAE mice also exhibited a marked increase in tdT^+ and $tdT^+Gal\text{-}3^+$ cells (Figures S7I–S7K). Super-resolution microscopy revealed a diverse composition of myeloid cells within the VI, including tdT^+ cells, $Gal\text{-}3^+$ cells, and $tdT^+Gal\text{-}3^+$ cells. Notably, several tdT^+IBA1^+ cells in the brain parenchyma of EAE mice exhibit microglial-like morphology, suggesting that tdT^+ cells may engraft and differentiate into macrophages during EAE (Figures S7L, S7L1, and S7L2). Together, these findings indicate that specific subsets of myeloid cells, such as $CCR2^+$ and Ms4a3-derived myeloid cells, utilize the VI to gain entry into the brain parenchyma during EAE.

In JHMV-infected mouse brains,[94,95] another established model of demyelination, we examined myeloid cells trafficking through the VI at 3 and 7 days post-infection (Figures S7M and S7N). At 3 days, $Gal\text{-}3^+$ staining was observed near

(B) CS of EAE mice plotted over time.
(C) Whole-brain images of MBP (white) staining in control and EAE mice.
(D) Quantification of (C).
(E) Whole-brain images of EAE mice at CS 1–3 stained for IBA1 (red); inset shows $IBA1^+$ cells in the VI.
(F and G) Quantification of $IBA1^+$ cells in the whole brain (F) and VI (G).
(H) EAE induction in $Cx3cr1^{GFP/+}Ccr2^{RFP/+}$ mice. Animals were euthanized at CS 2 (days 11–17).
(I) Whole-brain images of control and EAE $Cx3cr1^{GFP/+}Ccr2^{RFP/+}$ mice at CS2, stained for GFP ($CX3CR1^+$, green) and RFP ($CCR2^+$, red).
(J and K) Quantification of $CX3CR1^+$ and $CCR2^+$ cells in the whole brain (J) and VI (K).
(L) Quantification of (M).
(M) Meningeal whole mounts and confocal images of $CX3CR1^+$ and $CCR2^+$ cells in the dura mater; inset shows the SSS.
(N) Super-resolution images of brains from control and EAE mice stained for GFP (green), RFP (red), and LAMININ (blue). Insets (N1–N4) show $CCR2^+$ cells (arrows) within, near, and exiting the basement membrane of the VI under control (N1) and EAE (N2) conditions, illustrating various strategies of cell migration into the CNS parenchyma (N2–N4).
(O) Images of $CX3CR1^+$ (green), $CCR2^+$ (red), and LAMININ (blue) staining in the Lm and ChP in EAE mice.
(P) Quantification of $CCR2^+$ cells that expand from the VI, Lm, and ChP into adjacent brain parenchyma.
Data are mean ± SEM ($n = 5$–11; 2 groups: t test; 3+ groups: two-way ANOVA with Šidák's post hoc; $^*p < 0.05$, $^{***}p < 0.001$).
Scale bar: ∼200 μm for (C); ∼160 μm for (E), (I), and (M, whole brain and dura mater); ∼40 μm for (E, white insets); ∼60 μm for (M, white insets); ∼30 μm for (N) and (O); ∼20 μm for (N1); ∼10 μm for (N2)–(N4).
See also Figures S6 and S7.

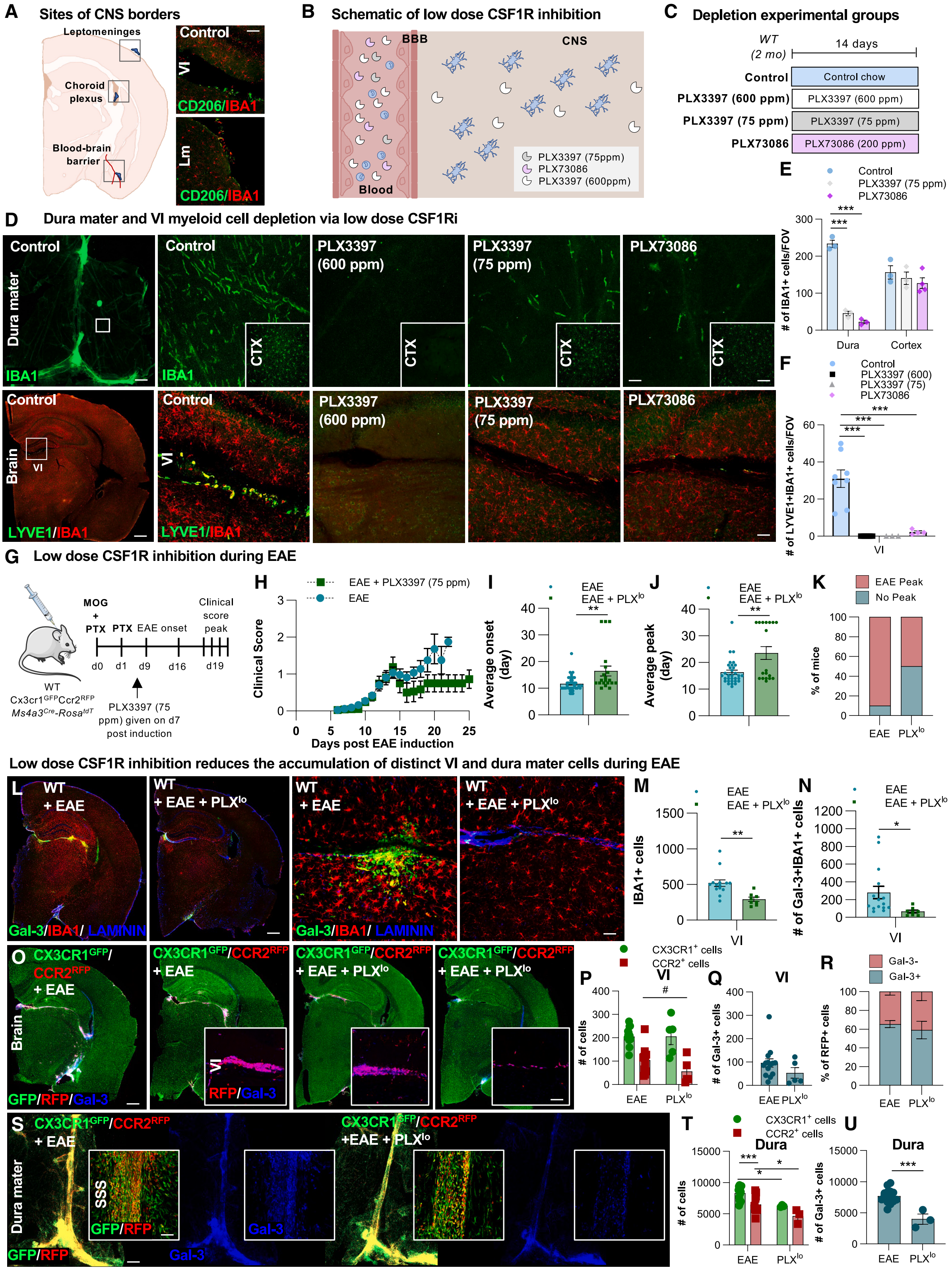

(legend on next page)

]

Please cite this article in press as: Hohsfield et al., Identification of the velum interpositum as a meningeal-CNS route for myeloid cell trafficking into the brain, Neuron (2025), https://doi.org/10.1016/j.neuron.2025.05.004

ventricular areas, with limited Gal-3$^+$ cell deposition in the VI (Figures S7O–S7S). At 7 days, Gal-3$^+$ cell accumulation was extensive in the CNS tissues surrounding the ventricles and white matter (WM) areas (Figures S7O–S7S). These findings indicate that myeloid cell trafficking via the VI is disease context dependent.

Low-dose CSF1Ri: A novel method for selective CNS macrophage depletion

To explore the role of the meninges and VI in CNS myeloid cell trafficking, we developed an approach to selectively deplete meningeal macrophages, a subset of BAMs (Figure 6A). Previous studies have shown that BAMs are dependent on CSF1R signaling for survival and function.[6,15] Taking advantage of the differential BBB penetration properties of CSF1Ri, we identified two compounds that could selectively eliminate BAMs, without affecting microglia: PLX3397 (75 ppm) and PLX73086 (200 pm). PLX3397 has ~5% plasma-CNS penetration, and at 75 ppm, it provides peripheral CSF1R inhibition exposure without parenchymal CNS penetration.[24] PLX73086 does not cross the BBB (Figure 6B).[96] Two-month-old mice were treated for 14 days with CSF1Ri, and brains and dura mater were collected for evaluation (Figure 6C). Immunostaining for IBA1 reveals that low-dose PLX3397 (75 ppm) or PLX73086 (200 ppm) treatment significantly reduces dural macrophages and VI myeloid cells without affecting microglial numbers (Figures 6D–6F).

Evaluation of BAM-specific markers CD206 and LYVE1[6,13,61–63] shows that CD206$^+$IBA1$^+$ cells are extensively distributed within all BAM compartments—leptomeninges, perivascular spaces, choroid plexus, as well as the VI (Figures 6A and S8A–S8H); while LYVE1$^+$IBA1$^+$ cells appear localized to meningeal regions, including the VI and leptomeninges (Figures 6D and S8I–S8K). Low-dose CSF1Ri treatment results in significant loss of CD206$^+$IBA1$^+$ and LYVE1$^+$IBA1$^+$ cells in the VI, leptomeninges, and choroid plexus (Figures S8A–S8D and S8G–S8L), while CD206$^+$IBA1$^+$ perivascular macrophages remain intact following PLX3397 (75 ppm). Single-cell transcriptional analysis and fate-mapping studies have revealed the presence of distinct macrophage CNS populations with differential origins.[7,16,97] Given this, we postulate that the differential impact of CSF1Ri on BAM subsets could reflect differential sensitivity to CSF1R inhibition or reliance on distinct signaling pathways for survival and proliferation. Together, these data indicate that the VI contains similar properties and dependencies as the dura mater, leptomeninges, and choroid plexus, suggesting they may belong or be connected to similar anatomical structures. Furthermore, these data demonstrate that PLX3397 (75 ppm) treatment can serve as a viable method for VI/meningeal-associated macrophage depletion.

Low-dose CSF1R inhibition during demyelinating disease

We next investigated the impact of low-dose CSF1R inhibition during demyelinating disease using PLX3397 (75 ppm). Three cohorts (WT, Cx3cr1$^{GFP/+}$Ccr2$^{RFP/+}$, and *Ms4a3*^{Cre}-*Rosa*^{TdT}) of mice were induced with EAE (Figures 6G, 6H, and S9A–S9C) and treated with PLX3397 (75 ppm) or vehicle diet starting 7 days post-induction (Figure 6G). While PLX3397 (75 ppm) did not significantly affect overall EAE score (Figure S9D), treated mice exhibited a significantly longer time to disease symptom onset and peak (Figures 6I and 6J). Moreover, a higher proportion of treated mice never progressed to the peak of EAE disease (i.e., 50% of mice never reached CS2+) (Figure 6K). These data suggest that VI-associated macrophage depletion may delay disease progression. Next, we evaluated the effects of low-dose CSF1Ri on distinct subsets of myeloid cells in the CNS during EAE. Here, we show that PLX3397 (75 ppm) did not impact parenchymal myeloid cell numbers, as assessed by IBA1$^+$, CX3CR1$^+$, and CCR2$^+$ (Figures S9E–S9H) but reduced specific VI and dural myeloid cell subsets. In WT EAE mice, IBA1$^+$ and Gal-3$^+$IBA1$^+$ cells were significantly reduced in the VI

Figure 6. Low-dose CSF1R inhibition during demyelinating disease

(A) Sites of CNS borders and macrophages. Immunofluorescence images of CD206$^+$ (green) and IBA1$^+$ (red) cells in the Lm and VI.

(B) Schematic of CSF1Ri distribution in blood and CNS.

(C) Experimental paradigm: WT mice were treated for 14 days with vehicle, PLX3397 (600 ppm), low-dose PLX3397 (75 ppm) or PLX73086 (200 ppm).

(D) Meningeal whole mount and higher-resolution images of IBA1$^+$ cells in the dura mater (top) and whole-brain and higher-resolution images of LYVE1$^+$ and IBA1$^+$ cells in the VI (lower); insets show IBA1$^+$ staining in the cortex.

(E and F) Quantification of (D).

(G) Three cohorts of 2- to 9-month-old female mice (WT, $n = 22$; Cx3cr1$^{GFP/+}$Ccr2$^{RFP/+}$, $n = 21$; and *Ms4a3*^{Cre}-*RosaTdT*, $n = 13$) were injected with MOG$_{35–55}$/CFA and PTX to induce EAE. PLX3397 (75 ppm) was administered at day 7 and continued until sacrifice. First signs of paralysis appeared at days 8–13. Animals were euthanized at CS $\geq$2 (days 11–19).

(H) CS of EAE mice treated with ($n = 19$) and without ($n = 37$) PLX3397 (75 ppm) plotted over time.

(I and J) Quantification of time to EAE onset (CS $\geq$ 0.5; I) and peak (CS $\geq$ 2; J) in control and PLX3397 75 ppm treated (PLX^{lo}) EAE mice.

(K) Percentage of mice that progress to the EAE peak (CS $\geq$ 2) and never progress to peak (CS $\leq$ 2).

(L) Images of Gal-3$^+$ (green), IBA1$^+$ (red), and LAMININ$^+$ (blue) staining in the whole brains and VI of WT EAE and PLX^{lo} treated EAE mice.

(M and N) Quantification of IBA1$^+$ cells (M) and Gal-3$^+$IBA1$^+$ (N) cells in the VI.

(O) Images of GFP$^+$ (CX3CR1$^+$, green), RFP$^+$ (CCR2$^+$, red), and Gal-3$^+$ (blue) staining in the whole brains and VI (insets) of Cx3cr1$^{GFP/+}$Ccr2$^{RFP/+}$ EAE with and without PLX^{lo} treatment.

(P and Q) Quantification of CX3CR1-GFP$^+$, CCR2-RFP$^+$ (P), and Gal-3$^+$ (Q) cells in the VI.

(R) Percentage of Gal-3$^+$RFP$^+$ and Gal-3$^-$RFP$^+$ cells in the VI.

(S) Images of GFP$^+$ (green), RFP$^+$ (red), and Gal-3$^+$ (blue) staining in the whole dura mater and the SSS (insets).

(T and U) Quantification of CX3CR1-GFP$^+$, CCR2-RFP$^+$ (T), and Gal-3$^+$ (U) cells in the dura mater.

Data are mean ± SEM ($n = 3$–39; 2 groups: t test; 3+ groups: one-way ANOVA with Šidák's post hoc; $^{\#}p < 1$; $^{*}p < 0.05$, $^{**}p < 0.01$, $^{***}p < 0.001$).

Scale bar: ~200 μm for (D), (L), (O), and (S, whole brain and dura mater); ~150 μm for (D, insets); ~70 μm for (A); ~50 μm for (D, bottom) and (L, right); ~40 μm for (D, bottom) and (O, insets); ~30 μm for (S, insets).

See also Figures S8 and S9.

Please cite this article in press as: Hohsfield et al., Identification of the velum interpositum as a meningeal-CNS route for myeloid cell trafficking into the brain, Neuron (2025), https://doi.org/10.1016/j.neuron.2025.05.004

(Figures 6L–6N). In Cx3cr1$^{GFP/+}$Ccr2$^{RFP/+}$ EAE mice, we observe a significant reduction in CX3CR1^{GFP+}, CCR2^{RFP+} (Figures 6O–6T), and Gal-3^{+} (Figures 6S and 6U) cells in the dura mater, particularly in the SSS (Figure 6S insets). In *Ms4a3^{Cre}-RosaTdT* EAE mice, we observed a trend toward reduction in Ms4a3-derived (tdT^{+}) IBA1^{+} cells in the brain (p = 0.056) (Figure S9I). Interestingly, animals reaching EAE disease peak displayed higher numbers of tdT^{+}IBA1^{+} cells in the VI compared with those that did not reach EAE peak (Figures S9J and S9K), indicating that tdT^{+}IBA1^{+} VI cell accumulation may be associated with EAE disease peak. Similar to Cx3cr1$^{GFP/+}$Ccr2$^{RFP/+}$ mice, IBA1^{+}, Ms4a3-derived (tdT^{+}), and Gal-3^{+} cells are significantly depleted in the dura mater following PLX3397 (75 ppm) (Figures S9L–S9O). Together, our study identifies low-dose CSF1R inhibition as a novel way to deplete distinct CNS macrophage populations and inhibit cell trafficking through the meningeal-VI route, which may have important therapeutic implications for neurological diseases involving aberrant immune cell infiltration into the CNS and brain.

DISCUSSION

Although previously considered a relatively inert, protective CNS barrier, evidence suggests that the meninges is a dynamic and immunologically active structure with important immune surveillance and defense functions,[4,8] including myeloid cell recruitment and infiltration.[44,45] In this study, we identified a specialized leptomeningeal structure that projects into the extra-parenchymal space of the murine brain bearing remarkable anatomical resemblance to the VI and transcriptional resemblance to VLMCs. Through lineage tracing, we confirm the occupancy of BAMs and peripheral myeloid cells within this structure. Importantly, we demonstrate that under certain conditions, myeloid cells can utilize this route for entry into the brain.

While the BBB typically restricts peripheral cell and molecule entry into the brain parenchyma, recent studies reveal close interactions between the periphery, CSF, skull, meninges, and CNS.[45,98] Louveau et al. identified meningeal lymphatics as important drainage routes for immune cells.[62,99] *In vivo* cell imaging of murine stroke and meningitis models reveal neutrophil migration from the skull BM to the brain surface through microscopic vascular channels.[45] Nanobody(V$_{H}$H)-boosted 3D imaging of solvent-cleared organs (vDISCO) imaging identified short vascular connections between the skull BM and meninges, which become filled with immune cells after middle cerebral artery occlusion.[53] Cugarra et al. report that many myeloid cells in the brain and spinal cord dura originate from skull and vertebral BM, and that skull BM-dura channels provide a route for myeloid migration from these skull BM pools.[46] During EAE, immune cells were seen migrating along bridging veins and crossing between the dura and SAS, identifying a potential route for myeloid cell trafficking during neuroinflammation.[98]

Previous anatomical studies report that meningeal extensions penetrate parenchymal tissue as large projections between major brain structures, as sheaths surrounding penetrating blood vessels, and the choroid plexus stroma.[54] The two largest folded structures of dura mater are the falx cerebri, which descends into the longitudinal fissure between the two cerebral hemispheres, and the tentorium, which separates the cerebral lobes from the cerebellum. Of interest, most of the dural sinuses are found adjacent to the falx cerebri and tentorium. Given its spatial proximity and myeloid composition, the VI may be connected to these dural infoldings and associated dural sinuses. In line with our study, a LAMININ^{+} and N-sulfated heparan sulfate^{+} meningeal projection extends under the hippocampus, where it is continuous with the choroid plexus stroma and forms the non-neuronal roofs of the ventricles.[54,100,101] Furthermore, intra-meningeal injection with dextran dye labels not the leptomeninges, as well as the tissue beneath the murine hippocampus.[100,101] Recently, Smyth et al. identified ACE points where bridging veins cross the arachnoid barrier and drain blood to the dural sinuses. We hypothesize that the VI's proximity to these ACE points may allow barrier-free myeloid cell trafficking. LAMININ staining is found around and in the cells that form ACE points, suggesting laminin may play a role in mediating myeloid cell trafficking at these sites.[44]

The processes underlying myeloid cell recruitment and entry into the CNS remain largely unknown. Two emerging mechanisms include glycocalyx-associated vascular-immune interactions and endothelial basement membrane (laminin)-driven infiltration.[90] We show that myeloid cells within the VI express CD206 that together with other glycans contributes to the glycocalyx, a pericellular matrix that regulates immune cell adhesion and rolling.[90] Separately, previous studies indicate that laminins 411 and 511, expressed on endothelial basement membranes, are critically involved in peripheral myeloid cell recruitment and differentiation.[45] Here, we show that the VI is a laminin-enriched structure, and that BM-derived cells (expressing MMP2) are mobilized within this structure under homeostatic and head-irradiated conditions. Immune cell migration across the glia limitans is mediated by tumor necrosis factor alpha (TNF-α) expression and activation of MMP2 and MMP9 for cleavage of α-dystroglcan, an ECM receptor on astrocytic endfeet.[99] Recently, it was also shown that MMP25 confers brain invasiveness by cleaving meningeal fibroblast-derived collagen, which allows endothelial tip cells to migrate across the pial basement membrane.[45] Together, these data indicate that laminin endothelial cells in the VI may provide cues for myeloid cell trafficking and that myeloid cells may use MMPs to migrate across this structure and glia limitans.

Accumulating evidence reinforces the potential utility of the meninges as a gateway for immune cell trafficking into the CNS. In this study, we characterize the VI, a specialized leptomeningeal structure that enables myeloid cell trafficking into the brain parenchyma. In line with this, previous studies highlight this route in murine models of pancreatic cancer, neurocysticercosis, EAE, and traumatic brain injury.[102–105] We hypothesize that the VI represents a unique site where leptomeningeal vessels (potentially arteries from the SAS that are surrounded by a pial sheath) project (positioned near ACE points, and/or dural infoldings/sinuses) into the extra-parenchymal brain space, allowing myeloid cells to crawl along blood vessels before entering (via cues from endothelial cells of the VI) the CNS parenchyma. Further research is needed to determine whether this structure becomes compromised under disease conditions, to identify the cell adhesion and chemokine signaling pathways involved in this infiltration, and to elucidate the distinct roles each of the

VI's leptomeningeal and vascular components in myeloid cell trafficking.

Our findings shed light on the cooperative and dynamic interactions of the brain and meninges in myeloid cell trafficking, as well as provide evidence for a neuroanatomical route of myeloid cell entry into the brain.

Limitations of this study

While our study offers insight into the VI's role in myeloid cell entry and migration into the brain parenchyma, limitations in current intravital imaging techniques prevent direct observation of active cell trafficking. Future research is needed to definitively determine the extent of myeloid cell trafficking, extravasation, and movement from the VI into the brain parenchymal space.

RESOURCE AVAILABILITY

Lead contact

Requests for further information and resources should be directed to and will be fulfilled by the lead contact, Kim Green (kngreen@uci.edu).

Materials availability

This study did not generate new unique reagents.

Data and code availability

All data reported in this paper will be shared by the lead contact upon request. This paper does not report original code. Any additional information required to reanalyze the data reported in this paper is available from the lead contact upon request.

ACKNOWLEDGMENTS

We thank Brian L. West and Andrey Rymar at Plexxikon, Inc. for providing and formulating CSF1Ri chow. We are grateful to Joshua D. Crapser for his critical input and editing of the manuscript. This work was supported by the National Institutes of Health (NIH) under awards: R01NS083801 (NINDS), R01AG056768 (NIA), R01AG081599 (NIA), and U54AG054349 (NIA Model Organism Development and Evaluation for Late-onset Alzheimer's Disease [MODEL-AD]) to K.N.G.; T32NS082174 (NINDS) to Y.G.; T32NS082174 (NINDS) to K.I.T.; T32NS121727 (NINDS) to N.E.K.; F31AG072852 (NIA) to C.M.H.; R35NS116835 (NINDS) to T.E.L.; and 1S10MH124715-01 (NIMH) to X.X.; L.A.H. was supported by the Alzheimer's Association Research Fellowship (AARF-16-442762). Graphical abstract was created in BioRender. Hohsfield, L. (2025) https://BioRender.com/zmnwc0g.

AUTHOR CONTRIBUTIONS

L.A.H. designed, conducted, and analyzed experiments, interpreted the results, and wrote the manuscript. S.J.K. conducted and analyzed experiments and performed bioinformatic analysis. R.A.B., C.M.H., and Y.G. conducted and analyzed experiments. K.M. and K.D.V. analyzed experiments. K.I.T., J.A.A.A., P.G., and C.P. conducted experiments. N.E.K. wrote the bioinformatics analysis pipeline. M.A.I., C.M.W., X.X., and T.E.L. contributed to project design. K.N.G. directed the project, designed the experiments, interpreted the results, and wrote the manuscript.

DECLARATION OF INTERESTS

The authors declare no competing interests.

STAR★METHODS

Detailed methods are provided in the online version of this paper and include the following:

- KEY RESOURCES TABLE
- EXPERIMENTAL MODEL AND SUBJECT DETAILS
  - ○ Animals
- METHOD DETAILS
  - ○ Colony-stimulating factor 1 receptor (CSF1R) inhibitor compounds
  - ○ CSF1R inhibitor-mediated microglial and CNS macrophage depletion
  - ○ Bone marrow transplant
  - ○ Flow cytometry
  - ○ Brain tissue collection and processing
  - ○ Dura mater tissue isolation
  - ○ Spatial proteomics and transcriptomics
  - ○ Spatial proteomics and transcriptomics data analysis
  - ○ Immunostaining and confocal microscopy
  - ○ Brain Clearing
  - ○ Light-Sheet Microscopy and 3D Reconstruction
  - ○ Models of demyelinating disease
- QUANTIFICATION AND STATISTICAL ANALYSIS
  - ○ Data analysis and statistics

SUPPLEMENTAL INFORMATION

Supplemental information can be found online at https://doi.org/10.1016/j.neuron.2025.05.004.

Received: July 28, 2024
Revised: February 28, 2025
Accepted: May 5, 2025
Published: June 3, 2025

REFERENCES

1. Prinz, M., and Priller, J. (2014). Microglia and brain macrophages in the molecular age: from origin to neuropsychiatric disease. Nat. Rev. Neurosci. *15*, 300–312. https://doi.org/10.1038/nrn3722.
2. Li, Q., and Barres, B.A. (2018). Microglia and macrophages in brain homeostasis and disease. Nat. Rev. Immunol. *18*, 225–242. https://doi.org/10.1038/nri.2017.125.
3. Kierdorf, K., and Prinz, M. (2017). Microglia in steady state. J. Clin. Invest. *127*, 3201–3209. https://doi.org/10.1172/JCI90602.
4. Kierdorf, K., Masuda, T., Jordão, M.J.C., and Prinz, M. (2019). Macrophages at CNS interfaces: ontogeny and function in health and disease. Nat. Rev. Neurosci. *20*, 547–562. https://doi.org/10.1038/s41583-019-0201-x.
5. Prinz, M., Erny, D., and Hagemeyer, N. (2017). Ontogeny and homeostasis of CNS myeloid cells. Nat. Immunol. *18*, 385–392. https://doi.org/10.1038/ni.3703.
6. Mrdjen, D., Pavlovic, A., Hartmann, F.J., Schreiner, B., Utz, S.G., Leung, B.P., Lelios, I., Heppner, F.L., Kipnis, J., Merkler, D., et al. (2018). High-Dimensional Single-Cell Mapping of Central Nervous System Immune Cells Reveals Distinct Myeloid Subsets in Health, Aging, and Disease. Immunity *48*, 380–395.e6. https://doi.org/10.1016/j.immuni.2018.01.011.
7. Masuda, T., Amann, L., Monaco, G., Sankowski, R., Staszewski, O., Krueger, M., Del Gaudio, F., He, L., Paterson, N., Nent, E., et al. (2022). Specification of CNS macrophage subsets occurs postnatally in defined niches. Nature *604*, 740–748. https://doi.org/10.1038/s41586-022-04596-2.
8. Schonhoff, A.M., Figge, D.A., Williams, G.P., Jurkuvenaite, A., Gallups, N.J., Childers, G.M., Webster, J.M., Standaert, D.G., Goldman, J.E., and Harms, A.S. (2023). Border-associated macrophages mediate the neuroinflammatory response in an alpha-synuclein model of Parkinson disease. Nat. Commun. *14*, 3754. https://doi.org/10.1038/s41467-023-39060-w.
9. Ajami, B., Bennett, J.L., Krieger, C., Tetzlaff, W., and Rossi, F.M.V. (2007). Local self-renewal can sustain CNS microglia maintenance and

function throughout adult life. Nat. Neurosci. *10*, 1538–1543. https://doi.org/10.1038/nn2014.

10. Askew, K., Li, K., Olmos-Alonso, A., Garcia-Moreno, F., Liang, Y., Richardson, P., Tipton, T., Chapman, M.A., Riecken, K., Beccari, S., et al. (2017). Coupled Proliferation and Apoptosis Maintain the Rapid Turnover of Microglia in the Adult Brain. Cell Rep. *18*, 391–405. https://doi.org/10.1016/j.celrep.2016.12.041.
11. Füger, P., Hefendehl, J.K., Veeraraghavalu, K., Wendeln, A.C., Schlosser, C., Obermüller, U., Wegenast-Braun, B.M., Neher, J.J., Martus, P., Kohsaka, S., et al. (2017). Microglia turnover with aging and in an Alzheimer's model via long-term in vivo single-cell imaging. Nat. Neurosci. *20*, 1371–1376. https://doi.org/10.1038/nn.4631.
12. Tay, T.L., Savage, J.C., Hui, C.W., Bisht, K., and Tremblay, M.È. (2017). Microglia across the lifespan: from origin to function in brain development, plasticity and cognition. J. Physiol. *595*, 1929–1945. https://doi.org/10.1113/JP272134.
13. Goldmann, T., Wieghofer, P., Jordão, M.J.C., Prutek, F., Hagemeyer, N., Frenzel, K., Amann, L., Staszewski, O., Kierdorf, K., Krueger, M., et al. (2016). Origin, fate and dynamics of macrophages at central nervous system interfaces. Nat. Immunol. *17*, 797–805. https://doi.org/10.1038/ni.3423.
14. Prinz, M., and Priller, J. (2017). The role of peripheral immune cells in the CNS in steady state and disease. Nat. Neurosci. *20*, 136–144. https://doi.org/10.1038/nn.4475.
15. Van Hove, H., Martens, L., Scheyltjens, I., De Vlaminck, K., Pombo Antunes, A.R., De Prijck, S., Vandamme, N., De Schepper, S., Van Isterdael, G., Scott, C.L., et al. (2019). A single-cell atlas of mouse brain macrophages reveals unique transcriptional identities shaped by ontogeny and tissue environment. Nat. Neurosci. *22*, 1021–1035. https://doi.org/10.1038/s41593-019-0393-4.
16. Utz, S.G., See, P., Mildenberger, W., Thion, M.S., Silvin, A., Lutz, M., Ingelfinger, F., Rayan, N.A., Lelios, I., Buttgereit, A., et al. (2020). Early Fate Defines Microglia and Non-parenchymal Brain Macrophage Development. Cell *181*, 557–573.e18. https://doi.org/10.1016/j.cell.2020.03.021.
17. Green, K.N., Crapser, J.D., and Hohsfield, L.A. (2020). To Kill a Microglia: A Case for CSF1R Inhibitors. Trends Immunol. *41*, 771–784. https://doi.org/10.1016/j.it.2020.07.001.
18. Spangenberg, E.E., and Green, K.N. (2017). Inflammation in Alzheimer's disease: Lessons learned from microglia-depletion models. Brain Behav. Immun. *61*, 1–11. https://doi.org/10.1016/j.bbi.2016.07.003.
19. Waisman, A., Ginhoux, F., Greter, M., and Bruttger, J. (2015). Homeostasis of Microglia in the Adult Brain: Review of Novel Microglia Depletion Systems. Trends Immunol. *36*, 625–636. https://doi.org/10.1016/j.it.2015.08.005.
20. Hohsfield, L.A., Najafi, A.R., Ghorbanian, Y., Soni, N., Hingco, E.E., Kim, S.J., Jue, A.D., Swarup, V., Inlay, M.A., and Green, K.N. (2020). Effects of long-term and brain-wide colonization of peripheral bone marrow-derived myeloid cells in the CNS. J. Neuroinflammation *17*, 279. https://doi.org/10.1186/s12974-020-01931-0.
21. Varvel, N.H., Grathwohl, S.A., Baumann, F., Liebig, C., Bosch, A., Brawek, B., Thal, D.R., Charo, I.F., Heppner, F.L., Aguzzi, A., et al. (2012). Microglial repopulation model reveals a robust homeostatic process for replacing CNS myeloid cells. Proc. Natl. Acad. Sci. USA *109*, 18150–18155. https://doi.org/10.1073/pnas.1210150109.
22. Bruttger, J., Karram, K., Wörtge, S., Regen, T., Marini, F., Hoppmann, N., Klein, M., Blank, T., Yona, S., Wolf, Y., et al. (2015). Genetic Cell Ablation Reveals Clusters of Local Self-Renewing Microglia in the Mammalian Central Nervous System. Immunity *43*, 92–106. https://doi.org/10.1016/j.immuni.2015.06.012.
23. Xu, Z., Rao, Y., Huang, Y., Zhou, T., Feng, R., Xiong, S., Yuan, T.F., Qin, S., Lu, Y., Zhou, X., et al. (2020). Efficient Strategies for Microglia Replacement in the Central Nervous System. Cell Rep. *32*, 108041. https://doi.org/10.1016/j.celrep.2020.108041.
24. Elmore, M.R.P., Najafi, A.R., Koike, M.A., Dagher, N.N., Spangenberg, E.E., Rice, R.A., Kitazawa, M., Matusow, B., Nguyen, H., West, B.L., et al. (2014). Colony-stimulating factor 1 receptor signaling is necessary for microglia viability, unmasking a microglia progenitor cell in the adult brain. Neuron *82*, 380–397. https://doi.org/10.1016/j.neuron.2014.02.040.
25. Huang, Y., Xu, Z., Xiong, S., Sun, F., Qin, G., Hu, G., Wang, J., Zhao, L., Liang, Y.X., Wu, T., et al. (2018). Repopulated microglia are solely derived from the proliferation of residual microglia after acute depletion. Nat. Neurosci. *21*, 530–540. https://doi.org/10.1038/s41593-018-0090-8.
26. Cronk, J.C., Filiano, A.J., Louveau, A., Marin, I., Marsh, R., Ji, E., Goldman, D.H., Smirnov, I., Geraci, N., Acton, S., et al. (2018). Peripherally derived macrophages can engraft the brain independent of irradiation and maintain an identity distinct from microglia. J. Exp. Med. *215*, 1627–1647. https://doi.org/10.1084/jem.20180247.
27. Lund, H., Pieber, M., Parsa, R., Han, J., Grommisch, D., Ewing, E., Kular, L., Needhamsen, M., Espinosa, A., Nilsson, E., et al. (2018). Competitive repopulation of an empty microglial niche yields functionally distinct subsets of microglia-like cells. Nat. Commun. *9*, 4845. https://doi.org/10.1038/s41467-018-07295-7.
28. Hohsfield, L.A., Najafi, A.R., Ghorbanian, Y., Soni, N., Crapser, J., Figueroa Velez, D.X., Jiang, S., Royer, S.E., Kim, S.J., Henningfield, C.M., et al. (2021). Subventricular zone/white matter microglia reconstitute the empty adult microglial niche in a dynamic wave. eLife *10*, e66738. https://doi.org/10.7554/eLife.66738.
29. Zhan, L., Krabbe, G., Du, F., Jones, I., Reichert, M.C., Telpoukhovskaia, M., Kodama, L., Wang, C., Cho, S.H., Sayed, F., et al. (2019). Proximal recolonization by self-renewing microglia re-establishes microglial homeostasis in the adult mouse brain. PLoS Biol. *17*, e3000134. https://doi.org/10.1371/journal.pbio.3000134.
30. Hammond, B.P., Manek, R., Kerr, B.J., Macauley, M.S., and Plemel, J.R. (2021). Regulation of microglia population dynamics throughout development, health, and disease. Glia *69*, 2771–2797. https://doi.org/10.1002/glia.24047.
31. Bennett, F.C., Bennett, M.L., Yaqoob, F., Mulinyawe, S.B., Grant, G.A., Hayden Gephart, M., Plowey, E.D., and Barres, B.A. (2018). A Combination of Ontogeny and CNS Environment Establishes Microglial Identity. Neuron *98*, 1170–1183.e8. https://doi.org/10.1016/j.neuron.2018.05.014.
32. Mildner, A., Schmidt, H., Nitsche, M., Merkler, D., Hanisch, U.K., Mack, M., Heikenwalder, M., Brück, W., Priller, J., and Prinz, M. (2007). Microglia in the adult brain arise from Ly-6ChiCCR2+ monocytes only under defined host conditions. Nat. Neurosci. *10*, 1544–1553. https://doi.org/10.1038/nn2015.
33. Peake, K., Manning, J., Lewis, C.A., Barr, C., Rossi, F., and Krieger, C. (2015). Busulfan as a myelosuppressive agent for generating stable high-level bone marrow chimerism in mice. J. Vis. Exp. e52553. https://doi.org/10.3791/52553.
34. Priller, J., Flügel, A., Wehner, T., Boentert, M., Haas, C.A., Prinz, M., Fernández-Klett, F., Prass, K., Bechmann, I., de Boer, B.A., et al. (2001). Targeting gene-modified hematopoietic cells to the central nervous system: use of green fluorescent protein uncovers microglial engraftment. Nat. Med. *7*, 1356–1361. https://doi.org/10.1038/nm1201-1356.
35. Simard, A.R., and Rivest, S. (2004). Bone marrow stem cells have the ability to populate the entire central nervous system into fully differentiated parenchymal microglia. FASEB J. *18*, 998–1000. https://doi.org/10.1096/fj.04-1517fje.
36. Han, J., Sarlus, H., Wszolek, Z.K., Karrenbauer, V.D., and Harris, R.A. (2020). Microglial replacement therapy: a potential therapeutic strategy for incurable CSF1R-related leukoencephalopathy. Acta Neuropathol. Commun. *8*, 217. https://doi.org/10.1186/s40478-020-01093-3.
37. Shibuya, Y., Kumar, K.K., Mader, M.M.D., Yoo, Y., Ayala, L.A., Zhou, M., Mohr, M.A., Neumayer, G., Kumar, I., Yamamoto, R., et al. (2022). Treatment of a genetic brain disease by CNS-wide microglia replacement.

Please cite this article in press as: Hohsfield et al., Identification of the velum interpositum as a meningeal-CNS route for myeloid cell trafficking into the brain, Neuron (2025), https://doi.org/10.1016/j.neuron.2025.05.004

Sci. Transl. Med. *14*, eabl9945. https://doi.org/10.1126/scitranslmed.abl9945.

38. Colella, P., Sayana, R., Suarez-Nieto, M.V., Sarno, J., Nyame, K., Xiong, J., Pimentel Vera, L.N., Arozqueta Basurto, J., Corbo, M., Limaye, A., et al. (2024). CNS-wide repopulation by hematopoietic-derived microglia-like cells corrects progranulin deficiency in mice. Nat. Commun. *15*, 5654. https://doi.org/10.1038/s41467-024-49908-4.
39. Marchetti, L., and Engelhardt, B. (2020). Immune cell trafficking across the blood-brain barrier in the absence and presence of neuroinflammation. Vasc. Biol. *2*, H1–H18. https://doi.org/10.1530/VB-19-0033.
40. Greiner, T., and Kipp, M. (2021). What Guides Peripheral Immune Cells into the Central Nervous System? Cells *10*, 2041. https://doi.org/10.3390/cells10082041.
41. Amann, L., Masuda, T., and Prinz, M. (2023). Mechanisms of myeloid cell entry to the healthy and diseased central nervous system. Nat. Immunol. *24*, 393–407. https://doi.org/10.1038/s41590-022-01415-8.
42. Bartholomäus, I., Kawakami, N., Odoardi, F., Schläger, C., Miljkovic, D., Ellwart, J.W., Klinkert, W.E.F., Flügel-Koch, C., Issekutz, T.B., Wekerle, H., et al. (2009). Effector T cell interactions with meningeal vascular structures in nascent autoimmune CNS lesions. Nature *462*, 94–98. https://doi.org/10.1038/nature08478.
43. Schläger, C., Körner, H., Krueger, M., Vidoli, S., Haberl, M., Mielke, D., Brylla, E., Issekutz, T., Cabañas, C., Nelson, P.J., et al. (2016). Effector T-cell trafficking between the leptomeninges and the cerebrospinal fluid. Nature *530*, 349–353. https://doi.org/10.1038/nature16939.
44. Smyth, L.C.D., Xu, D., Okar, S.V., Dykstra, T., Rustenhoven, J., Papadopoulos, Z., Bhasiin, K., Kim, M.W., Drieu, A., Mamuladze, T., et al. (2024). Identification of direct connections between the dura and the brain. Nature *627*, 165–173. https://doi.org/10.1038/s41586-023-06993-7.
45. Herisson, F., Frodermann, V., Courties, G., Rohde, D., Sun, Y., Vandoorne, K., Wojtkiewicz, G.R., Masson, G.S., Vinegoni, C., Kim, J., et al. (2018). Direct vascular channels connect skull bone marrow and the brain surface enabling myeloid cell migration. Nat. Neurosci. *21*, 1209–1217. https://doi.org/10.1038/s41593-018-0213-2.
46. Cugurra, A., Mamuladze, T., Rustenhoven, J., Dykstra, T., Beroshvili, G., Greenberg, Z.J., Baker, W., Papadopoulos, Z., Drieu, A., Blackburn, S., et al. (2021). Skull and vertebral bone marrow are myeloid cell reservoirs for the meninges and CNS parenchyma. Science *373*, eabf7844. https://doi.org/10.1126/science.abf7844.
47. Mapunda, J.A., Tibar, H., Regragui, W., and Engelhardt, B. (2022). How Does the Immune System Enter the Brain? Front. Immunol. *13*, 805657. https://doi.org/10.3389/fimmu.2022.805657.
48. Ginhoux, F., and Guilliams, M. (2016). Tissue-Resident Macrophage Ontogeny and Homeostasis. Immunity *44*, 439–449. https://doi.org/10.1016/j.immuni.2016.02.024.
49. Krasemann, S., Madore, C., Cialic, R., Baufeld, C., Calcagno, N., El Fatimy, R., Beckers, L., O'Loughlin, E., Xu, Y., Fanek, Z., et al. (2017). The TREM2-APOE Pathway Drives the Transcriptional Phenotype of Dysfunctional Microglia in Neurodegenerative Diseases. Immunity *47*, 566–581.e9. https://doi.org/10.1016/j.immuni.2017.08.008.
50. Safaiyan, S., Besson-Girard, S., Kaya, T., Cantuti-Castelvetri, L., Liu, L., Ji, H., Schifferer, M., Gouna, G., Usifo, F., Kannaiyan, N., et al. (2021). White matter aging drives microglial diversity. Neuron *109*, 1100–1117.e10. https://doi.org/10.1016/j.neuron.2021.01.027.
51. Hammond, T.R., Dufort, C., Dissing-Olesen, L., Giera, S., Young, A., Wysoker, A., Walker, A.J., Gergits, F., Segel, M., Nemesh, J., et al. (2019). Single-Cell RNA Sequencing of Microglia throughout the Mouse Lifespan and in the Injured Brain Reveals Complex Cell-State Changes. Immunity *50*, 253–271.e6. https://doi.org/10.1016/j.immuni.2018.11.004.
52. Hohsfield, L.A., Tsourmas, K.I., Ghorbanian, Y., Syage, A.R., Jin Kim, S., Cheng, Y., Furman, S., Inlay, M.A., Lane, T.E., and Green, K.N. (2022). MAC2 is a long-lasting marker of peripheral cell infiltrates into the mouse CNS after bone marrow transplantation and coronavirus infection. Glia *70*, 875–891. https://doi.org/10.1002/glia.24144.
53. Decimo, I., Dolci, S., Panuccio, G., Riva, M., Fumagalli, G., and Bifari, F. (2021). Meninges: A Widespread Niche of Neural Progenitors for the Brain. Neuroscientist *27*, 506–528. https://doi.org/10.1177/1073858420954826.
54. Decimo, I., Fumagalli, G., Berton, V., Krampera, M., and Bifari, F. (2012). Meninges: from protective membrane to stem cell niche. Am. J. Stem Cells *1*, 92–105.
55. Bifari, F., Decimo, I., Pino, A., Llorens-Bobadilla, E., Zhao, S., Lange, C., Panuccio, G., Boeckx, B., Thienpont, B., Vinckier, S., et al. (2017). Neurogenic Radial Glia-like Cells in Meninges Migrate and Differentiate into Functionally Integrated Neurons in the Neonatal Cortex. Cell Stem Cell *20*, 360–373.e7. https://doi.org/10.1016/j.stem.2016.10.020.
56. Funaki, T., Makino, Y., Arakawa, Y., Hojo, M., Kunieda, T., Takagi, Y., Takahashi, J.C., and Miyamoto, S. (2012). Arachnoid cyst of the velum interpositum originating from tela choroidea. Surg. Neurol. Int. *3*, 120. https://doi.org/10.4103/2152-7806.102334.
57. Rhoton, A.L., Jr. (2002). The lateral and third ventricles. Neurosurgery *51*, S207–S271. https://doi.org/10.1097/00006123-200210001-00006.
58. Zohdi, A., and Elkheshin, S. (2012). Endoscopic anatomy of the velum interpositum: A sequential descriptive anatomical study. Asian J. Neurosurg. *7*, 12–16. https://doi.org/10.4103/1793-5482.95689.
59. Nagata, S., Rhoton, A.L., Jr., and Barry, M. (1988). Microsurgical anatomy of the choroidal fissure. Surg. Neurol. *30*, 3–59. https://doi.org/10.1016/0090-3019(88)90180-2.
60. Jordão, M.J.C., Sankowski, R., Brendecke, S.M., Sagar, L., Locatelli, G., Tai, Y.H., Tay, T.L., Schramm, E., Armbruster, S., Hagemeyer, N., et al. (2019). Single-cell profiling identifies myeloid cell subsets with distinct fates during neuroinflammation. Science *363*, eaat7554. https://doi.org/10.1126/science.aat7554.
61. Faraco, G., Park, L., Anrather, J., and Iadecola, C. (2017). Brain perivascular macrophages: characterization and functional roles in health and disease. J. Mol. Med. (Berl.) *95*, 1143–1152. https://doi.org/10.1007/s00109-017-1573-x.
62. Louveau, A., Smirnov, I., Keyes, T.J., Eccles, J.D., Rouhani, S.J., Peske, J.D., Derecki, N.C., Castle, D., Mandell, J.W., Lee, K.S., et al. (2015). Structural and functional features of central nervous system lymphatic vessels. Nature *523*, 337–341. https://doi.org/10.1038/nature14432.
63. Zeisel, A., Muñoz-Manchado, A.B., Codeluppi, S., Lönnerberg, P., La Manno, G., Juréus, A., Marques, S., Munguba, H., He, L., Betsholtz, C., et al. (2015). Brain structure. Cell types in the mouse cortex and hippocampus revealed by single-cell RNA-seq. Science *347*, 1138–1142. https://doi.org/10.1126/science.aaa1934.
64. He, S., Bhatt, R., Brown, C., Brown, E.A., Buhr, D.L., Chantranuvatana, K., Danaher, P., Dunaway, D., Garrison, R.G., Geiss, G., et al. (2022). High-plex imaging of RNA and proteins at subcellular resolution in fixed tissue by spatial molecular imaging. Nat. Biotechnol. *40*, 1794–1806. https://doi.org/10.1038/s41587-022-01483-z.
65. Yu, X., Ng, C.P., Habacher, H., and Roy, S. (2008). Foxj1 transcription factors are master regulators of the motile ciliogenic program. Nat. Genet. *40*, 1445–1453. https://doi.org/10.1038/ng.263.
66. Zeisel, A., Hochgerner, H., Lönnerberg, P., Johnsson, A., Memic, F., van der Zwan, J., Häring, M., Braun, E., Borm, L.E., La Manno, G., et al. (2018). Molecular Architecture of the Mouse Nervous System. Cell *174*, 999–1014.e22. https://doi.org/10.1016/j.cell.2018.06.021.
67. Di Bella, D.J., Habibi, E., Stickels, R.R., Scalia, G., Brown, J., Yadollahpour, P., Yang, S.M., Abbate, C., Biancalani, T., Macosko, E.Z., et al. (2021). Molecular logic of cellular diversification in the mouse cerebral cortex. Nature *595*, 554–559. https://doi.org/10.1038/s41586-021-03670-5.

68. Tasic, B., Yao, Z., Graybuck, L.T., Smith, K.A., Nguyen, T.N., Bertagnolli, D., Goldy, J., Garren, E., Economo, M.N., Viswanathan, S., et al. (2018). Shared and distinct transcriptomic cell types across neocortical areas. Nature *563*, 72–78. https://doi.org/10.1038/s41586-018-0654-5.

69. Chen, Q., Leshkowitz, D., Blechman, J., and Levkowitz, G. (2020). Single-Cell Molecular and Cellular Architecture of the Mouse Neurohypophysis. eNeuro *7*, ENEURO.0345-19.2019. https://doi.org/10.1523/ENEURO.0345-19.2019.

70. Marques, S., Zeisel, A., Codeluppi, S., van Bruggen, D., Mendanha Falcão, A., Xiao, L., Li, H., Häring, M., Hochgerner, H., Romanov, R.A., et al. (2016). Oligodendrocyte heterogeneity in the mouse juvenile and adult central nervous system. Science *352*, 1326–1329. https://doi.org/10.1126/science.aaf6463.

71. Vanlandewijck, M., He, L., Mäe, M.A., Andrae, J., Ando, K., Del Gaudio, F., Nahar, K., Lebouvier, T., Laviña, B., Gouveia, L., et al. (2018). A molecular atlas of cell types and zonation in the brain vasculature. Nature *554*, 475–480. https://doi.org/10.1038/nature25739.

72. Pietilä, R., Del Gaudio, F., He, L., Vázquez-Liébanas, E., Vanlandewijck, M., Muhl, L., Mocci, G., Bjørnholm, K.D., Lindblad, C., Fletcher-Sandersjöö, A., et al. (2023). Molecular anatomy of adult mouse leptomeninges. Neuron *111*, 3745–3764.e7. https://doi.org/10.1016/j.neuron.2023.09.002.

73. DeSisto, J., O'Rourke, R., Jones, H.E., Pawlikowski, B., Malek, A.D., Bonney, S., Guimiot, F., Jones, K.L., and Siegenthaler, J.A. (2020). Single-Cell Transcriptomic Analyses of the Developing Meninges Reveal Meningeal Fibroblast Diversity and Function. Dev. Cell *54*, 43–59.e4. https://doi.org/10.1016/j.devcel.2020.06.009.

74. Shah, T., Leurgans, S.E., Mehta, R.I., Yang, J., Galloway, C.A., de Mesy Bentley, K.L., Schneider, J.A., and Mehta, R.I. (2023). Arachnoid granulations are lymphatic conduits that communicate with bone marrow and dura-arachnoid stroma. J. Exp. Med. *220*, e20220618. https://doi.org/10.1084/jem.20220618.

75. Kearns, N.A., Iatrou, A., Flood, D.J., De Tissera, S., Mullaney, Z.M., Xu, J., Gaiteri, C., Bennett, D.A., and Wang, Y. (2023). Dissecting the human leptomeninges at single-cell resolution. Nat. Commun. *14*, 7036. https://doi.org/10.1038/s41467-023-42825-y.

76. De Schepper, S., Ge, J.Z., Crowley, G., Ferreira, L.S.S., Garceau, D., Toomey, C.E., Sokolova, D., Rueda-Carrasco, J., Shin, S.H., Kim, J.S., et al. (2023). Perivascular cells induce microglial phagocytic states and synaptic engulfment via SPP1 in mouse models of Alzheimer's disease. Nat. Neurosci. *26*, 406–415. https://doi.org/10.1038/s41593-023-01257-z.

77. Dorrier, C.E., Jones, H.E., Pintarić, L., Siegenthaler, J.A., and Daneman, R. (2022). Emerging roles for CNS fibroblasts in health, injury and disease. Nat. Rev. Neurosci. *23*, 23–34. https://doi.org/10.1038/s41583-021-00525-w.

78. Albertini, R., and Bianchi, R. (2010). Aquaporins and glia. Curr. Neuropharmacol. *8*, 84–91. https://doi.org/10.2174/157015910791233178.

79. Hannocks, M.J., Pizzo, M.E., Huppert, J., Deshpande, T., Abbott, N.J., Thorne, R.G., and Sorokin, L. (2018). Molecular characterization of perivascular drainage pathways in the murine brain. J. Cereb. Blood Flow Metab. *38*, 669–686. https://doi.org/10.1177/0271678X17749689.

80. Agrawal, S., Anderson, P., Durbeej, M., van Rooijen, N., Ivars, F., Opdenakker, G., and Sorokin, L.M. (2006). Dystroglycan is selectively cleaved at the parenchymal basement membrane at sites of leukocyte extravasation in experimental autoimmune encephalomyelitis. J. Exp. Med. *203*, 1007–1019. https://doi.org/10.1084/jem.20051342.

81. Rua, R., and McGavern, D.B. (2018). Advances in Meningeal Immunity. Trends Mol. Med. *24*, 542–559. https://doi.org/10.1016/j.molmed.2018.04.003.

82. Herz, J., Filiano, A.J., Wiltbank, A.T., Yogev, N., and Kipnis, J. (2017). Myeloid Cells in the Central Nervous System. Immunity *46*, 943–956. https://doi.org/10.1016/j.immuni.2017.06.007.

83. Russo, M.V., Latour, L.L., and McGavern, D.B. (2018). Distinct myeloid cell subsets promote meningeal remodeling and vascular repair after mild traumatic brain injury. Nat. Immunol. *19*, 442–452. https://doi.org/10.1038/s41590-018-0086-2.

84. Derk, J., Jones, H.E., Como, C., Pawlikowski, B., and Siegenthaler, J.A. (2021). Living on the Edge of the CNS: Meninges Cell Diversity in Health and Disease. Front. Cell. Neurosci. *15*, 703944. https://doi.org/10.3389/fncel.2021.703944.

85. Kierdorf, K., Erny, D., Goldmann, T., Sander, V., Schulz, C., Perdiguero, E.G., Wieghofer, P., Heinrich, A., Riemke, P., Hölscher, C., et al. (2013). Microglia emerge from erythromyeloid precursors via Pu.1- and Irf8-dependent pathways. Nat. Neurosci. *16*, 273–280. https://doi.org/10.1038/nn.3318.

86. Prinz, M., Masuda, T., Wheeler, M.A., and Quintana, F.J. (2021). Microglia and Central Nervous System-Associated Macrophages-From Origin to Disease Modulation. Annu. Rev. Immunol. *39*, 251–277. https://doi.org/10.1146/annurev-immunol-093019-110159.

87. Bridlance, C., and Thion, M.S. (2023). Multifaceted microglia during brain development: Models and tools. Front. Neurosci. *17*, 1125729. https://doi.org/10.3389/fnins.2023.1125729.

88. Stremmel, C., Schuchert, R., Wagner, F., Thaler, R., Weinberger, T., Pick, R., Mass, E., Ishikawa-Ankerhold, H.C., Margraf, A., Hutter, S., et al. (2018). Yolk sac macrophage progenitors traffic to the embryo during defined stages of development. Nat. Commun. *9*, 75. https://doi.org/10.1038/s41467-017-02492-2.

89. Arnoux, I., Hoshiko, M., Mandavy, L., Avignone, E., Yamamoto, N., and Audinat, E. (2013). Adaptive phenotype of microglial cells during the normal postnatal development of the somatosensory "Barrel" cortex. Glia *61*, 1582–1594. https://doi.org/10.1002/glia.22503.

90. Dalmau Gasull, A., Glavan, M., Samawar, S.K.R., Kapupara, K., Kelk, J., Rubio, M., Fumagalli, S., Sorokin, L., Vivien, D., and Prinz, M. (2024). The niche matters: origin, function and fate of CNS-associated macrophages during health and disease. Acta Neuropathol. *147*, 37. https://doi.org/10.1007/s00401-023-02676-9.

91. Bernardo-Castro, S., Sousa, J.A., Brás, A., Cecília, C., Rodrigues, B., Almendra, L., Machado, C., Santo, G., Silva, F., Ferreira, L., et al. (2020). Pathophysiology of Blood-Brain Barrier Permeability Throughout the Different Stages of Ischemic Stroke and Its Implication on Hemorrhagic Transformation and Recovery. Front. Neurol. *11*, 594672. https://doi.org/10.3389/fneur.2020.594672.

92. Mildner, A., Schlevogt, B., Kierdorf, K., Böttcher, C., Erny, D., Kummer, M.P., Quinn, M., Brück, W., Bechmann, I., Heneka, M.T., et al. (2011). Distinct and non-redundant roles of microglia and myeloid subsets in mouse models of Alzheimer's disease. J. Neurosci. *31*, 11159–11171. https://doi.org/10.1523/JNEUROSCI.6209-10.2011.

93. Liu, Z., Gu, Y., Chakarov, S., Bleriot, C., Kwok, I., Chen, X., Shin, A., Huang, W., Dress, R.J., Dutertre, C.A., et al. (2019). Fate Mapping via Ms4a3-Expression History Traces Monocyte-Derived Cells. Cell *178*, 1509–1525.e19. https://doi.org/10.1016/j.cell.2019.08.009.

94. Held, K.S., Chen, B.P., Kuziel, W.A., Rollins, B.J., and Lane, T.E. (2004). Differential roles of CCL2 and CCR2 in host defense to coronavirus infection. Virology *329*, 251–260. https://doi.org/10.1016/j.virol.2004.09.006.

95. Savarin, C., Stohlman, S.A., Atkinson, R., Ransohoff, R.M., and Bergmann, C.C. (2010). Monocytes regulate T cell migration through the glia limitans during acute viral encephalitis. J. Virol. *84*, 4878–4888. https://doi.org/10.1128/JVI.00051-10.

96. Bellver-Landete, V., Bretheau, F., Mailhot, B., Vallières, N., Lessard, M., Janelle, M.E., Vernoux, N., Tremblay, M.È., Fuehrmann, T., Shoichet, M. S., et al. (2019). Microglia are an essential component of the neuroprotective scar that forms after spinal cord injury. Nat. Commun. *10*, 518. https://doi.org/10.1038/s41467-019-08446-0.

97. Siret, C., van Lessen, M., Bavais, J., Jeong, H.W., Reddy Samawar, S.K., Kapupara, K., Wang, S., Simic, M., de Fabritus, L., Tchoghandjian, A., et al. (2022). Deciphering the heterogeneity of the Lyve1(+) perivascular

macrophages in the mouse brain. Nat. Commun. *13*, 7366. https://doi.org/10.1038/s41467-022-35166-9.

98. Cai, R., Pan, C., Ghasemigharagoz, A., Todorov, M.I., Förstera, B., Zhao, S., Bhatia, H.S., Parra-Damas, A., Mrowka, L., Theodorou, D., et al. (2019). Panoptic imaging of transparent mice reveals whole-body neuronal projections and skull-meninges connections. Nat. Neurosci. *22*, 317–327. https://doi.org/10.1038/s41593-018-0301-3.
99. Louveau, A., Herz, J., Alme, M.N., Salvador, A.F., Dong, M.Q., Viar, K.E., Herod, S.G., Knopp, J., Setliff, J.C., Lupi, A.L., et al. (2018). CNS lymphatic drainage and neuroinflammation are regulated by meningeal lymphatic vasculature. Nat. Neurosci. *21*, 1380–1391. https://doi.org/10.1038/s41593-018-0227-9.
100. Mercier, F., and Hatton, G.I. (2003). Meninges and perivasculature as mediators of CNS plasticity. In Advances in Molecular and Cell Biology (Elsevier), pp. 215–253. https://doi.org/10.1016/S1569-2558(03)31010-0.
101. Mercier, F., and Arikawa-Hirasawa, E. (2012). Heparan sulfate niche for cell proliferation in the adult brain. Neurosci. Lett. *510*, 67–72. https://doi.org/10.1016/j.neulet.2011.12.046.
102. Burfeind, K.G., Zhu, X., Norgard, M.A., Levasseur, P.R., Huisman, C., Buenafe, A.C., Olson, B., Michaelis, K.A., Torres, E.R., Jeng, S., et al. (2020). Circulating myeloid cells invade the central nervous system to mediate cachexia during pancreatic cancer. eLife *9*, e54095. https://doi.org/10.7554/eLife.54095.
103. Alvarez, J.I., and Teale, J.M. (2006). Breakdown of the blood brain barrier and blood-cerebrospinal fluid barrier is associated with differential leukocyte migration in distinct compartments of the CNS during the course of murine NCC. J. Neuroimmunol. *173*, 45–55. https://doi.org/10.1016/j.jneuroim.2005.11.020.
104. Schmitt, C., Strazielle, N., and Ghersi-Egea, J.F. (2012). Brain leukocyte infiltration initiated by peripheral inflammation or experimental autoimmune encephalomyelitis occurs through pathways connected to the CSF-filled compartments of the forebrain and midbrain. J. Neuroinflammation *9*, 187. https://doi.org/10.1186/1742-2094-9-187.
105. Szmydynger-Chodobska, J., Shan, R., Thomasian, N., and Chodobski, A. (2016). The Involvement of Pial Microvessels in Leukocyte Invasion after Mild Traumatic Brain Injury. PLoS One *11*, e0167677. https://doi.org/10.1371/journal.pone.0167677.
106. Saederup, N., Cardona, A.E., Croft, K., Mizutani, M., Cotleur, A.C., Tsou, C.L., Ransohoff, R.M., and Charo, I.F. (2010). Selective chemokine receptor usage by central nervous system myeloid cells in CCR2-red fluorescent protein knock-in mice. PLoS One *5*, e13693. https://doi.org/10.1371/journal.pone.0013693.
107. Jung, S., Aliberti, J., Graemmel, P., Sunshine, M.J., Kreutzberg, G.W., Sher, A., and Littman, D.R. (2000). Analysis of fractalkine receptor CX(3)CR1 function by targeted deletion and green fluorescent protein reporter gene insertion. Mol. Cell. Biol. *20*, 4106–4114. https://doi.org/10.1128/MCB.20.11.4106-4114.2000.
108. Connor, A.L., Kelley, P.M., and Tempero, R.M. (2016). Lymphatic endothelial lineage assemblage during corneal lymphangiogenesis. Lab Invest *96*, 270–282. https://doi.org/10.1038/labinvest.2015.147.
109. Canli, Ö., Nicolas, A.M., Gupta, J., Finkelmeier, F., Goncharova, O., Pesic, M., Neumann, T., Horst, D., Löwer, M., Sahin, U., et al. (2017). Myeloid Cell-Derived Reactive Oxygen Species Induce Epithelial Mutagenesis. Cancer Cell *32*, 869–883.e5. https://doi.org/10.1016/j.ccell.2017.11.004.
110. Madisen, L., Zwingman, T.A., Sunkin, S.M., Oh, S.W., Zariwala, H.A., Gu, H., Ng, L.L., Palmiter, R.D., Hawrylycz, M.J., Jones, A.R., et al. (2010). A robust and high-throughput Cre reporting and characterization system for the whole mouse brain. Nat. Neurosci. *13*, 133–140. https://doi.org/10.1038/nn.2467.
111. Okabe, M., Ikawa, M., Kominami, K., Nakanishi, T., and Nishimune, Y. (1997). 'Green mice' as a source of ubiquitous green cells. FEBS Lett. *407*, 313–319. https://doi.org/10.1016/s0014-5793(97)00313-x.
112. Hao, Y., Stuart, T., Kowalski, M.H., Choudhary, S., Hoffman, P., Hartman, A., Srivastava, A., Molla, G., Madad, S., Fernandez-Granda, C., et al. (2024). Dictionary learning for integrative, multimodal and scalable single-cell analysis. Nat. Biotechnol. *42*, 293–304. https://doi.org/10.1038/s41587-023-01767-y.
113. Connor, A.L., Kelley, P.M., and Tempero, R.M. (2016). Lymphatic endothelial lineage assemblage during corneal lymphangiogenesis. Lab. Invest. *96*, 270–282. https://doi.org/10.1038/labinvest.2015.147.
114. Tran, K.M., Kwang, N., Gomez-Arboledas, A., Kawauchi, S., Mar, C., Chao, D., Da Cunha, C., Wang, S., Collins, S., Walker, A., et al. (2024). APOE Christchurch enhances a disease-associated microglial response to plaque but suppresses response to tau pathology. Preprint at bioRxiv. https://doi.org/10.1101/2024.06.03.597211.
115. Zhang, W., Li, I., Reticker-Flynn, N.E., Good, Z., Chang, S., Samusik, N., Saumyaa, S., Li, Y., Zhou, X., Liang, R., et al. (2022). Identification of cell types in multiplexed in situ images by combining protein expression and spatial information using CELESTA. Nat. Methods *19*, 759–769. https://doi.org/10.1038/s41592-022-01498-z.
116. Wickham, H., and Wickham, H. (2016). Data Analysis (Springer).
117. Szklarczyk, D., Kirsch, R., Koutrouli, M., Nastou, K., Mehryary, F., Hachilif, R., Gable, A.L., Fang, T., Doncheva, N.T., Pyysalo, S., et al. (2023). The STRING database in 2023: protein-protein association networks and functional enrichment analyses for any sequenced genome of interest. Nucleic Acids Res. *51*, D638–D646. https://doi.org/10.1093/nar/gkac1000.
118. Elmore, M.R.P., Lee, R.J., West, B.L., and Green, K.N. (2015). Characterizing newly repopulated microglia in the adult mouse: impacts on animal behavior, cell morphology, and neuroinflammation. PLoS One *10*, e0122912. https://doi.org/10.1371/journal.pone.0122912.
119. Park, Y.G., Sohn, C.H., Chen, R., McCue, M., Yun, D.H., Drummond, G. T., Ku, T., Evans, N.B., Oak, H.C., Trieu, W., et al. (2018). Protection of tissue physicochemical properties using polyfunctional crosslinkers. Nat. Biotechnol. https://doi.org/10.1038/nbt.4281.
120. Yun, D.H., Park, Y.-G., Cho, J.H., Kamentsky, L., Evans, N.B., DiNapoli, N., Xie, K., Choi, S.W., Albanese, A., Tian, Y., et al. (2025). Uniform volumetric single-cell processing for organ-scale molecular phenotyping. Nat. Biotechnol. https://doi.org/10.1038/s41587-024-02533-4.

Please cite this article in press as: Hohsfield et al., Identification of the velum interpositum as a meningeal-CNS route for myeloid cell trafficking into the brain, Neuron (2025), https://doi.org/10.1016/j.neuron.2025.05.004

STAR★METHODS

KEY RESOURCES TABLE

REAGENT or RESOURCE	SOURCE	IDENTIFIER
Antibodies		
rabbit-anti-IBA1	FUJIFILM Wako Pure Chemical Corporation	Cat# 019-19741; RRID:AB_839504
goat-anti-IBA1	Abcam	Cat# ab5076; RRID:AB_2224402
chicken-anti-IBA1	Synaptic Systems	Cat# 234 009; RRID:AB_2891282
chicken-anti-GFP	Abcam	Cat# ab13970; RRID:AB_300798
rabbit-anti-GFP	Abcam	Cat# ab6556; RRID:AB_305564
rat-anti-MAC-2 and Gal-3	CEDARLANE	Cat# CL8942AP; RRID:AB_10060357
rat-anti-CD31	BD Biosciences	Cat# 550274; RRID:AB_393571
chicken-anti-GFAP	Abcam	Cat# ab4674; RRID:AB_304558
rabbit-anti-Laminin	Sigma-Aldrich	Cat# L9393; RRID:AB_477163
mouse-anti-TIE2	Abcam	Cat# ab24859; RRID:AB_2255983
rabbit-anti-LYVE1	Abcam	Cat# ab14917; RRID:AB_301509
goat-anti-DPPIV/CD26	R and D Systems	Cat# AF954; RRID:AB_355739
rabbit-anti-MMP2	Abcam	Cat# ab97779; RRID:AB_10696122
mouse-anti-NeuN	Sigma-Aldrich	Cat# MAB377; RRID:AB_2298772
rabbit-anti-RFP	Rockland	Cat# 600-401-379; RRID:AB_2209751
rat-anti-CD206	Bio-Rad	Cat# MCA2235GA; RRID:AB_322613
rat-anti-Laminin α1	Hannocks et al.[79]; a gift from L. Sorokin	N/A
rat-anti-Laminin α2	Hannocks et al.[79]; a gift from L. Sorokin	N/A
rat-anti-Laminin β1	Hannocks et al.[79]; a gift from L. Sorokin	N/A
rat-anti-Laminin γ1	Hannocks et al.[79]; a gift from L. Sorokin	N/A
anti-mouse CD11b APC	Biolegend	101212
anti-mouse Gr1 AF700	Biolegend	108422
anti-mouse CD45 APC/Cy7	Biolegend	103116
Bacterial and virus strains		
Neurotropic JHM strain of the mouse hepatitis virus (JHMV)		N/A
Chemicals, peptides, and recombinant proteins		
Tamoxifen	Sigma-Aldrich	Cat# 10540-29-1
Corn Oil	Sigma-Aldrich	Cat# C8267-500ML
Formaldehyde solution 4%, buffered, pH 6.9	Sigma-Aldrich	Cat# 1.00496.0700
Formalin, Neutral, Buffered 10% w/v in Phosphate Buffer	EMS Diasum	Cat# 15740
PBS - Phosphate-Buffered Saline (10X) pH 7.4	ThermoFisher	Cat# AM9625
TBS with Tween™ (TBST), 20X Solution	ThermoFisher	Cat# J77500.K2
10 mM Tris Base	FisherScientific	Cat# BP2471-500
1 mM EDTA	FisherScientific	Cat# S311-500
Tween 20	FisherScientific	Cat# BP337-500
4% sodium dodecyl sulfate	ThermoFisher	Cat# AM9822
DEPC-treated water	ThermoFisher	Cat# AM9922
50% deionized formamide	ThermoFisher	Cat# AM9342

(Continued on next page)

Please cite this article in press as: Hohsfield et al., Identification of the velum interpositum as a meningeal-CNS route for myeloid cell trafficking into the brain, Neuron (2025), https://doi.org/10.1016/j.neuron.2025.05.004

Continued

REAGENT or RESOURCE	SOURCE	IDENTIFIER
2X saline-sodium citrate	ThermoFisher	Cat# AM9763
Fluoromount-G	Southern Biotech	Cat# 0100-01
Fluoromount-G with DAPI	Invitrogen	Cat# 00-4959-52
Critical commercial assays		
Hooke Kits™ for EAE Induction in C57BL/6 Mice	Hooke Laboratories	Cat# EK-2110
Experimental models: Organisms/strains		
Mouse: *Wild-type C57BL/6*	The Jackson Laboratory	JAX 000664
Mouse: *Cx3cr1*$^{GFP/GFP}$*Ccr2*$^{RFP/RFP}$	Saederup et al.[106] and Jung et al.[107]	JAX 032127
Mouse: *Lyve1*^{CreERT2}	Connor et al.[108]; a gift from D. Fink	N/A
Mouse: *LysM*^{CreERT2}	Canli et al.[109]	JAX 031674
Mouse: *Ms4a3*^{Cre}	Liu et al.[93]	JAX 036382
Mouse: *Ai9 Rosa26*^{tdTomato}	Madisen et al.[110]	JAX 00790
Mouse: *CAG-EGFP*	Okabe et al.[111]	JAX 006567
Software and algorithms		
Imaris 7.5	Bitplane	https://imaris.oxinst.com
R (4.3.2)	The R Foundation	https://www.r-project.org
R package Seurat (5.1.0)	Hao et al.[112]	https://satijalab.org/seurat/index.html
ggplot2 (3.5.1)	The R Foundation	https://cran.r-project.org/web/packages/ggplot2/index.html
Las X	Leica Microsystems	https://www.leica-microsystems.com/products/microscope-software/p/leica-las-x-ls/
Zen Blue	Zeiss	https://www.zeiss.com/microscopy/us/products/software/zeiss-zen.html
FIJI	Open source	https://imagej.net/ij/; RRID: SCR_003070
Graph Pad Prism	GraphPad Software	https://www.graphpad.com
FlowJo	FlowJo	https://www.flowjo.com
SlideBook	3i Inc.	https://www.intelligent-imaging.com/slidebook

EXPERIMENTAL MODEL AND SUBJECT DETAILS

Animals

All rodent experiments were performed in accordance with animal protocols approved by the Institutional Animal Care and Use Committee at the University of California Irvine (UCI). All experiments involving mice comply with the Animal Research: Reporting of in Vivo Experiments (ARRIVE-10) guidelines. Experimental procedures were performed under anesthesia and all efforts were made to minimize suffering.

Animals were housed in autoclaved individual ventilated cages (SuperMouse 750, Lab Products) containing autoclaved corncob bedding (Envigo 7092BK 1/8'' Teklad) and two autoclaved 2'' square cotton nestlets (Ancare) plus a LifeSpan multi-level environmental enrichment platform. Animals were provided with tap water (acidified to pH2.5-3.0 with HCl then autoclaved) and food (LabDiet Mouse Irr 6F; LabDiet) *ad libitum*. Cages were changed every 2 weeks with a maximum of 5 adult animals per cage. Room temperature (RT) was maintained at 72 ± 2°F, with ambient room humidity (average 40-60% RH, range 10 - 70%). Light cycle was 14h light / 10h dark, lights on at 06.30h and off at 20.30h.

Both sexes were utilized for all experiments, except for EAE experiments, in which only female mice were used, in accordance with manufacturer recommendations. For all experiments, analyses were done using adult mice within the age span of 2-9 months.

Wild-type C57BL/6 (JAX 000664), and the following genetically modified mice were used: Cx3cr1$^{GFP/GFP}$Ccr2$^{RFP/RFP}$ (JAX 032127) mice were bred to C57BL/6 to obtain Cx3cr1$^{GFP/+}$Ccr2$^{RFP/+}$ mice. *Ccr2*^{RFP} and *Cx3cr1*^{GFP} mice have been previously described.[106,107] *Lyve1*^{CreERT2} mice[113] (gifted from Dr. Darci Fink), *LysM*^{CreERT2} (JAX 031674)[109] and *Ms4a3*^{Cre} (JAX 036382)[93] were bred to Ai9 *Rosa26*^{tdTomato} (JAX 007909) reporter mice. *Rosa*^{tdT} reporter mice have been previously described.[110] For transplant studies, bone marrow cells were isolated from CAG-EGFP mice (JAX 006567).[111] To obtain efficient conversion of *loxP* alleles and induce Cre recombination, adult (2-6 mo old) mice were given a dose of 5 mg tamoxifen/ 25 g animal body weight by oral gavage over

Please cite this article in press as: Hohsfield et al., Identification of the velum interpositum as a meningeal-CNS route for myeloid cell trafficking into the brain, Neuron (2025), https://doi.org/10.1016/j.neuron.2025.05.004

five consecutive days. Tamoxifen (10540-29-1, Sigma-Aldrich) was suspended in corn oil (C8267-500ML, Sigma-Aldrich) for 60 min at 50°C.

METHOD DETAILS

Colony-stimulating factor 1 receptor (CSF1R) inhibitor compounds

PLX3397 (pexidartinib) was synthesized following the published procedure (PMID: 26222558). PLX3397 and PLX73086 was provided by Plexxikon Inc. and formulated in AIN-76A standard chow by Research Diets Inc. at 600 ppm (PLX3397), 75 ppm (PLX3397) or 200 ppm (PLX73086).

CSF1R inhibitor-mediated microglial and CNS macrophage depletion

To deplete microglia, adult (2-9 mo old) male and female mice were administered ad libitum with pexidartinib (PLX3397) at a dosage of 600 ppm for 14 days. To stimulate microglial repopulation, PLX3397 was withdrawn and replaced with vehicle chow for duration of recovery period. For CNS macrophage depletion, mice were administered ad libitum with PLX3397 at a dosage of 75 ppm or PLX73086 at 200 ppm for 14 days or the duration of experiment.

Bone marrow transplant

Adult (2-6 mo old) male and female C57BL/6 mice were anesthetized with isoflurane and then irradiated with 1000 cGy (whole body [WB] or head-shielded [HS]) and reconstituted via retroorbital injection with 2 x 10^6 whole BM cells from CAG-EGFP mice (n=3 per group). Blood was measured at 12 weeks post transplantation to track granulocyte chimerism. WB and HS GFP-BM chimeric mice were treated with CSF1Ri treatment (PLX3397 600 ppm for 14d) 3 months following irradiation and then allowed to recover on control diet for 14d. For longer term recovery (~10 mo post irradiation) GFP-BM chimeric mice, animals were treated with CSF1Ri treatment (PLX3397 600 ppm for 14d) 3 months following irradiation and then allowed to recover on control diet for 6 mo (n=9). At the time of sacrifice, the mice were euthanized, and BM was harvested and analyzed by flow cytometry for HSC chimerism. This established an average percent chimerism of >95% in WB and >40% in HS irradiated mice.

Flow cytometry

Peripheral blood cells/granulocytes were collected from adult mice (5-7 mo of age) via the tail vein and placed in EDTA tubes. Blood samples were treated with ACK Lysis Buffer for 5 minutes at room temperature to lyse red blood cells. For bone marrow myeloid cell analysis, cells were stained with CD11b-APC (101212, Biolegend), Gr1-AF700 (108422, Biolegend), and CD45-APC/Cy7 (103116, Biolegend) antibodies at a dilution of 1:200 at 4°C for 15-30 min. Cells were maintained at 4°C and analyzed on a BD LSRII (BD Biosciences). Data were analyzed using FlowJo software.

Brain tissue collection and processing

Tissue was collected from terminally anesthetized (via carbon dioxide inhalation) mice by first perfusing through the left ventricle of the heart with ice-cold 1X phosphate-buffered saline (PBS). Brains were extracted and dissected down the midline, with one half flash-frozen for subsequent RNA and protein analyses, and the other half drop-fixed in 4% paraformaldehyde (1.00496.0700, Sigma-Aldrich). Fixed brains were cryopreserved in PBS + 0.05% sodium azide + 30% sucrose, frozen, and sectioned at 40 μm on a Leica SM2000 R sliding microtome. Brain sections between bregma -1.58 and -2.92 were used for subsequent immunohistochemical and spatial molecular imaging analyses. For mouse pups (below the age of postnatal day P9), animals were fully sedated using ice and then decapitated. Intact skulls were fixed and then decalcified by incubation in 10% HCl for 24 hours. After decalcification, samples were cryopreserved and brain + skull sections (20 μm) were generated using a cryostat (CM 1850-3-1, Leica Microsystems).

Dura mater tissue isolation

To isolate the dura mater of the meninges of adult mice (2–12 mo of age), the skull was cleaned of tissue and the lower portion removed. The brain was carefully removed, leaving the upper half of the skull with attached dura mater intact. The skullcap was placed in 4% PFA for two days and then placed in PBS + 0.05% sodium azide for one day or until harvest. Using a dissecting microscope, the dura mater was carefully removed by peeling the structure from the surface of the skull cap.

Spatial proteomics and transcriptomics

Brains were analyzed for 64 proteins and 1,000 genes using the CosMx Spatial Molecular Imager platform. Brain hemispheres from adult (6 mo old) wild-type C57BL/6 male and female mice (*n*=4, 2 per sex) were flash frozen in isopentane (-40°C) and kept at - 80°C until future use. Twenty-four to forty-eight hours prior to CosMx run, frozen brains were embedded in optimal cutting temperature (OCT) compound (Tissue-Tek, Sakura Fintek) and sliced into coronal sections at a 10-um thickness via cryostat (CM1950, LeicaBiosystems). Hemibrains (one from each mouse) were mounted onto a VWR Superfrost Plus microscope slide (48311-703, Avantor) and kept at - 80°C until fixation. Brain sections from the same mice were used for both proteomics and transcriptomics.

Please cite this article in press as: Hohsfield et al., Identification of the velum interpositum as a meningeal-CNS route for myeloid cell trafficking into the brain, Neuron (2025), https://doi.org/10.1016/j.neuron.2025.05.004

Slides were prepared according to manufacturer's recommendations (Bruker CosMx RNA and protein fresh frozen manual slide preparation) as previously detailed.[114] All reagents were obtained from Bruker CosMx kits unless otherwise indicated.

Spatial proteomics slide preparation

For fixation, slides were incubated in pre-cooled 10% neutral buffered formalin (NBF; 15740, EMS Diasum) for 2 hr at 4°C, washed three times in 1X PBS (diluted from 10X PBS, AM9625, ThermoFisher) for 5 min, baked in a baking oven (Model 10 Lab Oven, Quincy Lab) at 60°C for 30 min, then washed three times in 1X Tris Buffered Saline with Tween (TBS-T; J77500.K2, ThermoFisher) for 5 min. Antigen retrieval was performed in a pressure cooker (6-quart; BSB 7015, BioSB TintoRetriver) at 80°C in Tris-EDTA buffer (10 mM Tris Base [BP2471-500, FisherScientific], 1 mM EDTA solution [S311-500, ThermoFisher], 0.05% Tween 20 [BP337-500, FisherScientific], pH 9.0) for 7 min. After antigen retrieval, slides were cooled to RT for 5 minutes, then washed three times in 1X TBS-T for 5 min. For all subsequent steps, slides were placed in a humidity chamber (M920-2, Simport) unless otherwise indicated. As a blocking step, slides were incubated with Buffer W for 1 hr at RT. Next, slides were incubated with CosMx 64-plex protein panel and segmentation markers (GFAP, IBA1, NEUN, and S6) at 4°C for 16-18 hr (overnight). After overnight incubation with primary antibodies, slides were washed three times in 1X TBS-T for 10 min, then washed in 1X PBS for 2 min. Fiducials for image alignment were diluted to 0.00005% in 1X TBS-T and applied to the slide, then incubated for 5 min. For post-fixation, slides were washed in 1X PBS for 5 min, incubated in 4% PFA (1.00496.0700, Sigma-Aldrich) for 30 min, then washed three times in 1X PBS for 5 min. Slides were incubated in DAPI nuclear stain for 10 min, then washed twice in 1X PBS for 5 min. Slides were incubated in 100 mM NHS-Acetate for 15 min at RT and then submerged in 1X PBS for a minimum of 5 min. Flow cells were affixed to each slide, then loaded into the CosMx instrument (Bruker CosMx Spatial Molecular Imager). Approximately 350 FOVs were selected per slide, capturing the VI, hippocampus and cortical regions for each hemibrain section. Slides were imaged for 6 days and then uploaded to the Bruker AtoMx platform for analysis. Data visualization of each exported Seurat object file was performed using R 4.3.1.

Spatial transcriptomics slide preparation

For fixation, slides were immersed in 10% NBF for 2 hr at 4°C, washed three times in 1X PBS (pH 7.4) for 2 min, and baked at 60°C for 30 min. Slides were then washed and rehydrated as follows: three washes of 1X PBS for 5 min, 4% sodium dodecyl sulfate (SDS; AM9822, ThermoFisher) for 2 min, three washes of 1X PBS for 5 min, 50% ethanol for 5 min, 70% ethanol for 5 min, and two washes of 100% ethanol for 5 min, before air drying for 10 min at RT. Antigen retrieval was performed in a pressure cooker at 100°C for 15 min in 1X CosMx Target Retrieval Solution. Slides were immediately transferred to DEPC-treated water (AM9922, ThermoFisher) and washed for 15 sec, incubated in 100% ethanol for 3 min, then air-dried for ~30 min. For tissue permeabilization, each slide was incubated with digestion buffer (3 μg/mL proteinase K in 1X PBS) for 30 min at RT, then washed twice in 1X PBS for 5 min. Fiducials for image alignment were diluted to 0.00015% in 2X SSC-T, applied to the slide, and incubated for 5 min. For post-fixation, slides were processed in the following steps: 10% NBF for 1 min, two washes of NBF Stop Buffer (0.1M Tris-Glycine Buffer, 15740) for 5 min each, and 1x PBS for 5 min. All subsequent steps were performed in a humidity chamber. Next, NHS-Acetate (100 mM; 26777) mixture was applied to each slide and incubated for 15 min at RT. Slides were washed twice in 2X SSC for 5 min each. For *in situ* hybridization, slides were incubated with a modified 1000-plex Mouse Neuro RNA panel along with an rRNA segmentation marker in a hybridization/baking oven (HybEZ oven, ACDBio) at 37°C for 16-18 hr (overnight). Following *in situ* hybridization, slides were washed twice in a stringent wash solution (50% deionized formamide [AM9342, ThermoFisher], 2X saline-sodium citrate [SSC; AM9763, ThermoFisher]) at 37°C for 25 min, then twice in 2X SSC for 2 min. Slides were incubated in DAPI nuclear stain for 15 min, washed in 1X PBS for 5 min, incubated with GFAP and histone cell segmentation markers for 1 hr, then washed three times in 1X PBS for 5 min. Flow cells were affixed to each slide to create a fluidic channel for imaging, then loaded into the CosMx instrument. Approximately 350 FOVs were selected per slide, capturing the VI, hippocampal and cortical regions for each hemibrain section. Slides were imaged for 7 days and data were uploaded to the Bruker AtoMx platform. Pre-processed data was exported as a Seurat object for further analysis in R 4.3.1.

Spatial proteomics and transcriptomics data analysis

Spatial proteomics data analysis

Spatial proteomics data were filtered using the AtoMx Protein Quality Control module to flag unreliable cells based on segmented cell area, negative probe expression, and overly high/low protein expression. Mean fluorescence intensity data were hyperbolic arcsine transformed with the AtoMx Protein Normalization module. Cell types were automatically annotated based on marker gene expression using the CELESTA algorithm.[115] Images were captured from AtoMx platform.

Spatial transcriptomics data analysis

Spatial transcriptomics datasets were filtered using the AtoMx RNA Quality Control module to flag outlier negative probes (control probes targeting non-existent sequences to quantify non-specific hybridization), lowly-expressing cells, FOVs, and target genes. Datasets were then normalized and scaled using Seurat 5.0.1 *SCTransform* to account for differences in library size across cell types.[112] Principal component analysis (PCA) and uniform manifold approximation and projection (UMAP) analysis were performed to reduce dimensionality and visualize clusters in space. Transcript counts for each gene were acquired per cell. Unsupervised clustering at 0.5 resolution yielded 27 clusters. Differential gene expression analysis was performed by comparing each cluster to all other clusters in Seurat. Clusters were manually annotated based on gene expression and spatial location. Visualization of clusters in the x-y space were generated using ggplot2 3.4.4.[116] KEGG pathways for Cluster 12 genes were generated using string-db.org.[117]

Immunostaining and confocal microscopy

Fluorescent immunolabeling followed a standard indirect technique as described previously.[24] Coronal or sagittal free-floating brain sections washed with 1X PBS (1 x 5 min) and incubated in blocking solution (5% normal serum with 0.2% Triton X-100 in PBS) for 60 min. Sections were then stained against primary antibodies (diluted in blocking solution) at 4°C, with primary antibodies and dilutions used as follows: IBA1 (1:1000; 019-19741, Wako and ab5076, Abcam; 234 009, Synaptic systems), GFP (1:200, ab13970, Abcam), YFP/GFP (1:200, ab6556, Abcam), Gal-3 (1:500, CL8942AP, Cedarlane), CD31 (1:200, 550274, BD Pharmigen), GFAP (1:3000, ab4674, Abcam), LAMININ (1:50, L9393, Sigma), TIE2 (1:100, ab24859, Abcam), LYVE1 (1:200, ab14917, Abcam), DPP4 (1:200, R&D Systems, AF954), MMP2 (1:200, ab97779, Abcam), NeuN (1:1000; MAB377, EMD Millipore), RFP (1:200, 600-401-379, Rockland), and CD206 (1:100, MCA2235GA, Bio-Rad). Rat anti-mouse laminin $\alpha 1$ (#200, conditioned medium), rat anti-mouse laminin $\alpha 2$ (4H8-2, conditioned medium), rat anti-mouse laminin $\beta 1$ (3A4, conditioned medium), and rat anti-mouse laminin $\gamma 1$ (3E10, conditioned medium) were kind gifts from Dr. Lydia Sorokin.[79] Following primary antibody incubation, sections were washed with PBS (3 x 5–10 min) and then incubated in corresponding secondary antibodies (goat anti-mouse for mouse primary, goat anti-rabbit for rabbit primary antibody, etc.) for 1 hr covered. Sections were then washed with PBS (3x 10 min) covered. Sections were then mounted on slides and allowed to dry before cover-slipping with Fluoromount-G (0100-01, Southern Biotech). For DAPI staining, mounted brain sections were cover-slipped using Fluoromount-G with DAPI (00-4959-52, Invitrogen). High resolution fluorescent images were obtained using a Leica TCS SPE-II confocal microscope and LAS-X software. Image acquisition was done using 25x objectives and images were processes using LAS X (Leica) software. For confocal imaging, one field of view (FOV) per brain region was captured per mouse unless otherwise indicated. To capture whole brain stitches, automated slide scanning was performed using a Zeiss AxioScan.Z1 equipped with a Colibri camera and Zen AxioScan 2.3 software. Super-resolution fluorescent imaging was performed using a Zeiss LSM 900 microscope equipped with Airyscan 2. Data acquisition was conducted sequentially by tracks to optimize fluorescence channel separation, using a scan zoom of 0.70 and a bidirectional scan mode. For 20x imaging, a z-stack of 7 slices was collected over a 24 μm range with 4 μm intervals, resulting in an image size of 453.68 μm x 453.68 μm. For 63x imaging with an oil-immersion objective, a z-stack of 8 slices was collected over a 14 μm range with 2 μm intervals, yielding an image size of 144.03 μm x 144.03 μm. Super-resolution images were processed using Zeiss ZEN Blue software with Airyscan deconvolution. Microglial morphology was determined using the filaments module in Bitplane Imaris 7.5, as described previously.[118] Cell quantities were determined using the spots module in Imaris. Percent coverage measurements were determined in Image J (NIH). Dotted white lines of the VI were drawn based on distinct tissue architecture – a demarcation between the hippocampal and thalamic structures of the murine brain. This boundary was also determined by the presence of LAMININ$^+$, TIE2$^+$, and LYVE1$^+$ staining or the presence of distinct myeloid cells, such as LYVE1$^+$ or CCR2$^+$ cells within this structure.

Brain Clearing

Adult mice (2-6 mo old, n=2) were transcardially perfused with ice-cold PBS and whole brains drop-fixed 4% PFA in PBS for 12-24 hours. Brains were then stored in 1X PBS with 0.02% sodium azide at 4°C. Whole mouse brains were processed using clearing reagents and protocols from LifeCanvas Technologies (SB-FB25, Cambridge, MA). Briefly, whole brains were processed with the Clear + Pipeline by first incubating in SHIELD solution[119] for four days to preserve tissue structure and antigenicity. Following SHIELD preservation, brains underwent delipidation and clearing with the Clear+ tissue clearing method, utilizing the SmartBatch+ system[120] for rapid and uniform processing over two days. Active immunolabeling was performed with primary antibody LAMININ (10μg/whole brain, L9393, Sigma-Aldrich) and Cy5-conjugated secondary antibody (Cy™5 AffiniPure™ Donkey Anti-Rabbit IgG (H+L), 20 μg//whole brain, 711-295-152, Jackson Immunoresearch) in SmartBatch+ system. Finally, the samples were immersed in EasyIndex refractive index matching medium (EI-500-1.52) for two days to achieve optical transparency completing the Clear + Tissue Clearing Pipeline.

Light-Sheet Microscopy and 3D Reconstruction

Cleared whole mouse brains were imaged using the Cleared Tissue Light-Sheet (CTLS) microscope (3i Inc.) equipped with visible laser lines at 488, 561, and 670 nm. During imaging, the samples were submerged in EasyIndex refractive index matching medium. Illumination was provided by a tiling light-sheet system, and imaging was conducted with a 1.5×/0.25 NA objective lens. High-resolution 3D datasets were obtained with lateral resolutions of 1 μm per pixel and axial steps of 3 μm (captured at 1 μm x 1 μm x 3 μm voxel size). Raw data were saved as 16-bit TIFF files with lossless compression, and 3D visualizations were created using SlideBook (3i Inc.) and Imaris software. Maximum projection images were captured at size x: 3 μ, y: 3 μm, z: 3 μm. For videos, a series of 2,699 single TIFF images, acquired in the horizontal plane of the mouse brain using LightSheet Microscopy, were rendered in a 3D viewer using Imaris. The Ortho Slicer tool was used to computationally reconstruct a coronal view (XZ plane), generating a flythrough visualization from the most anterior to the most posterior coronal slices, providing a comprehensive view of the entire brain.

Models of demyelinating disease

Experimental Autoimmune Encephalomyelitis

On day of immunization (d0), female mice (C57BL/6 mice aged 9-13 weeks old [n=15]; Cx3cr1$^{GFP/+}$Ccr2$^{RFP/+}$ mice aged 2-5 mo [n=15]; Ms4a3^{Cre}-Rosa^{tdT} mice aged 8-9 mo [n=15]); were immunized by two subcutaneous injections with 100 μl of emulsion containing 100 μg of Myelin Oligodendrocyte Glycoprotein (MOG$_{35\text{-}55}$) with complete Freund's adjuvant (CFA) (EK-2110, Hooke

Please cite this article in press as: Hohsfield et al., Identification of the velum interpositum as a meningeal-CNS route for myeloid cell trafficking into the brain, Neuron (2025), https://doi.org/10.1016/j.neuron.2025.05.004

Laboratories). Two hours after MOG injections, mice received an intraperitoneal (ip) injection with 110 ng of pertussis toxin (PTX) from *Bordetella pertussis* (EK-2110, Hooke Laboratories) in sterile 1X PBS. Twenty-two to twenty-six hr after PTX injection, mice received another ip injection with 110 ng of PTX. Mice were monitored for clinical symptoms daily. Clinical evaluation was performed double-blind and based on the following scoring system; 0, asymptomatic; 0.5, ruffled fur; 1, flaccid tail; 2, hind limb paresis; 2.5, partial hind limb paralysis; 3, hind limb paralysis; 4, hind limb and forelimb paralysis; 5, moribund. Mice were sacrificed at clinical score 1, 2, and 3 for longitudinal analysis of myeloid cell activation and accumulation during EAE. For all other studies, mice were sacrificed at clinical score ≥ 2. Clinical score data is presented as average ± SEM.

Neurotropic JHM strain of the mouse hepatitis virus (JHMV)

Six- to eight-week-old C57BL/6 mice (males and females, n=9) were infected intracranially (ic) with 1100 PFU of JHMV in 30 μl of sterile Hanks balanced sterile solution (HBSS); control mice received an ic injection of HBSS. JHMV-infected C57BL/6 mice were sacrificed at 3- and 7-days post-infection (dpi) and brains isolated to assess viral titers and perform immunohistochemical staining.

QUANTIFICATION AND STATISTICAL ANALYSIS

Data analysis and statistics

Statistical analysis was performed with Graph Pad Prism (v10.0.1). To compare two groups, the unpaired Student's t-test was used. To compare multiple groups, a one-way or two-way ANOVA with Tukey's or Šidák's post hoc test was performed. For all analyses, statistical significance was accepted at $p < 0.05$. All bar graphs are represented as means +/- SEM and significance expressed as follows: *$p < 0.05$, **$p< 0.01$, ***$p < 0.001$. Statistical trends were accepted at $p < 0.10$ (# denotes trending significance). n is given as the number of mice within each group. The statistical analyses performed for each experiment are indicated in the figure legends. No statistical methods were used to predetermine sample size. The experiments were not randomized, and the investigators were not blinded to allocation during experiments and outcome assessment.